J. Fluid Mech. (2026), *vol.* 1028, A30, doi:10.1017/jfm.2025.11107

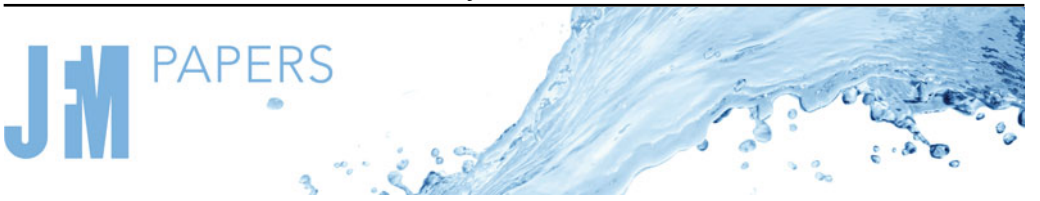

Scaling of drag forces on accelerating plates

Jesse Reijtenbagh[1], **Mark J. Tummers**[1] **and Jerry Westerweel**[1]

[1]Laboratory for Aero and Hydrodynamics, Delft University of Technology, Delft, The Netherlands

Corresponding author: Jesse Reijtenbagh, j.reijtenbagh@tudelft.nl

(Received 28 April 2025; revised 19 August 2025; accepted 16 December 2025)

Predicting unsteady loads on plate-like objects during unsteady motion is important in many applications, such as ship manoeuvring, flight and biological propulsion. The drag force on a starting plate that moves normal to its surface can be severely underestimated during the acceleration phase when conventional methods are used to incorporate the effects of acceleration. These methods often introduce an inviscid added mass force that has its origin in potential flow. However, the flow field around a starting plate quickly diverges from potential flow after the start of the motion due to the continuous creation of vorticity at the plate surface. Following the concept of drag by Burgers (1921 *Proc. K. Ned. Akad. Wet.* 23, 774–782), we propose a model to predict the creation of vorticity on the plate surface and its advection into the vortex loop at the plate edges, based on Stokes' first problem. This model shows that the acceleration drag force is a history force, in contrast to the inviscid added mass force that is proportional to the instantaneous acceleration of the plate. We perform experiments on starting plates over a large range of accelerations, velocities, fluid viscosities and plate geometries for which the model gives accurate predictions for the drag force during acceleration and during the relaxation phase immediately after the acceleration ceases. This model is extended to also predict the drag forces on accelerating plates during a starting motion with a non-constant acceleration.

Key words: flow-structure interactions, vortex flows, wakes

1. Introduction

The canonical problem of a starting object in a quiescent fluid has been investigated for more than a century, where the main focus has been on the force response and the starting vortices. An example is the early work of Prandtl (1936), who studied the starting vortex behind a wedge. The motion of an accelerating object in a fluid is relevant to various applications, such as the gust response of surging wings and wind turbine blades (Mancini

et al. 2015; Eldredge & Jones 2019), flapping insect wings (Dickinson, Lehmann & Sane 1999; Pullin & Wang 2004), ship manoeuvring and motion of offshore structures (Lighthill 1986) and also certain sports, such as the propulsion force generated by a rowing blade (Grift *et al.* 2019, 2021). When an object changes its velocity the kinetic energy of the surrounding fluid must also change. This change in kinetic energy requires work, which is interpreted as the work done by an 'added mass force' on the object (Batchelor 1967; Brennen 1982). In the case of an irrotational flow the added mass force can be computed through potential flow theory and scales linearly with acceleration. This is referred to as the inviscid added mass force. When the surrounding flow contains vorticity, it is often referred to as the circulatory force due to acceleration (e.g. Corkery, Stevens & Babinsky 2017), of which the scaling with respect to the motion of the object is not fully known.

Perhaps the most widely used expression for the force on an object that experiences a variation in velocity is the Morison equation (Morison *et al.* 1950). This equation separates the time-dependent drag force $F_D(t)$ on an object into a quasisteady drag force $F_{QS}(t)$ and an acceleration drag force $F_a(t)$,

$$F_D(t) = \underbrace{C_D \frac{1}{2}\rho V^2(t) A}_{F_{QS}(t)} + F_a(t), \tag{1.1}$$

where $V(t)$ is the instantaneous velocity of the object, C_D the steady-state drag coefficient, ρ the fluid density and A the frontal area of the object. The acceleration drag force $F_a(t)$ in the original Morison equation is taken equal to the inviscid added mass force $F_{AM} = m_h a(t)$, where the (time-dependent) acceleration $a(t)$ is multiplied by a constant hydrodynamic mass m_h, which is found from potential flow theory (Batchelor 1967; Brennen 1982) or determined empirically (Yu 1945; Payne 1981). When the flow is accelerating and the object is stationary, $F_a(t)$ includes the Froude–Krylov force (Lighthill 1986). Morison *et al.* (1950) originally considered a variation of fluid velocity due to small-amplitude linear wave motion, which is adequately described by potential flow. This justifies the use of the inviscid added mass force F_{AM} for F_a in the original equation. The use of F_{AM} is also justified for impulsive motions with a (nearly) instantaneous increase in velocity (e.g. von Kármán 1929), where the flow and its change in kinetic energy are adequately described by potential flow. Using an inviscid added mass force for separated and viscous flows, where the flow pattern changes during the acceleration, is questionable, as noted by both Batchelor (1967) and Brennen (1982).

Following Burgers (1921), an object that is brought into motion in a fluid generates a vortex layer at its surface that diffuses into the fluid due to the viscosity of the fluid, and is subsequently 'washed away' by the flow. Then, another vortex layer is formed that also diffuses away, and so on, where the rate per unit of time of impulse to create the subsequent vortex layers forms the drag force experienced by the moving body. The model of Reijtenbagh, Tummers & Westerweel (2023) is based on this concept, and is used later in this paper to describe the scaling of the force $F_a(t)$ for accelerating plates. Burgers (1921) subsequently derives an expression that relates the drag force on an object to the time derivative of the impulse of the fluid motion (see also Biesheuvel & Hagmeijer 2006). Wu (1981) and Lighthill (1986) arrive independently at the same expression, which is the basis of methods to determine the force on a moving object from the surrounding velocity field (Noca, Shields & Jeon 1997; Limacher, Morton & Wood 2018; Corkery, Babinsky & Graham 2019). Several studies have elucidated the role of vortical fluid motion in the resulting forces acting on instationary moving objects; here we focus on recent ones. Pitt Ford & Babinsky (2013) study the flow around an

accelerating plate in a towing tank to determine the inertial effect of the developing leading-edge vortex on the lift force. Fernando, Weymouth & Rival (2020) demonstrate that inviscid added mass force does not properly explain the force that acts on a circular plate in a constant-acceleration motion. Later, Reijtenbagh *et al.* (2023) find that the peak value of the acceleration drag force $F_a(t) = F_D(t) - F_{QS}(t)$ does not scale linearly with acceleration, as would be expected for the inviscid added mass force F_{AM}, but rather scales with the square root of the acceleration.

Alternative approaches to describe the acceleration drag force $F_a(t)$ in (1.1) have been suggested, such as the vortex force decomposition (Gehlert, Andreu-Angelo & Babinsky 2023) that divides the force into circulatory and non-circulatory components, the drift volume approach (McPhaden & Rival 2018) and impulse-based methods (Wu 1981; Lighthill 1986; Limacher *et al.* 2018). These methods can be considered data-driven, since they require knowledge of the flow field and flow structures surrounding the object to provide the forces on the moving object. Hence, these methods are not suited to provide an *a priori* scaling of the drag force with respect to the acceleration of the object. Also, these methods take vorticity to be already present, usually in the form of starting vortices and shear layers, but do not describe explicitly how this vorticity is created. Morton (1984) provides a summary on the generation of vorticity at a wall.

Besides experimental studies, there have been numerous numerical studies that focus on the drag force on and the flow field around accelerating and impulsively started plates. Koumoutsakos & Shiels (1996) use numerical simulations to investigate the vorticity field around a two-dimensional plate in an accelerating flow over a wide range of accelerations with Reynolds numbers between 20 and 1000. They show that the drag coefficients for different accelerations collapse on a single curve, indicating the possible existence of a general scaling law. Pullin & Wang (2004) use an inviscid model to describe the flow around an accelerating two-dimensional plate to obtain the unsteady forces that would mimic those of flapping insect wings. Later, Pullin & Sader (2021) studied the trailing edge vortex in an inviscid fluid by the start-up motion of a two-dimensional plate, with power laws for both the translational and rotational velocities. Hinton *et al.* (2024) extended their inviscid theory to an arbitrary two-dimensional body with sharp and straight edges, and formulated similarity solutions for the starting vortex at the trailing edges. Then, Sader *et al.* (2024) assessed the inviscid predictions using results from direct numerical simulations. Although related to the present work, their studies mainly focused on the lift force on pitching plates that have an initial small angle of attack, whereas the present work is on the drag force on three-dimensional plates accelerating in a direction normal to the plate surface. Xu & Nitsche (2014) propose scaling laws for impulsively started two-dimensional plates for Reynolds numbers between 250 and 2000, and later determine similar scaling laws for constant and non-constant accelerations (Xu & Nitsche 2015). Wang & Eldredge (2013) performed numerical simulations on impulsively started two-dimensional plates at various angles of attack using a viscous vortex particle method for a Reynolds number of 20 000. This low-order method closely resembles the creation and 'washing away' of vorticity described by Burgers (1921).

In this paper we explore the scaling of the acceleration drag force $F_a(t)$ on plates that accelerate from rest in a stagnant fluid. We consider different types of motion, where a plate undergoes a finite-duration acceleration phase until a certain final velocity is reached, for both constant and non-constant accelerations. This work extends previously reported findings that the original Morison equation, that includes the inviscid added mass, underestimates the actual drag force both during and immediately after the acceleration phase (Reijtenbagh *et al.* 2023). We measure the drag force on the plate during the entire motion, including a relaxation phase that follows the acceleration phase, where the drag

force gradually attains the steady motion drag force, as illustrated in figure 1(*a–d*) for various examples taken from the full set of measurements over various accelerations a and final velocities V_a. These examples illustrate the motivation behind this work. The same data is presented in figure 1(*e–h*), but now as a function of the dimensionless time t^*, defined as (Gharib, Rambod & Shariff 1998)

$$t^* = \frac{1}{\ell}\int_0^t V(\tau)\mathrm{d}\tau. \tag{1.2}$$

This is commonly referred to as the formation time, and it expresses the distance the plate has travelled since the start of the motion ($t = 0$) in terms of length ℓ. We have chosen the length ℓ to be equal to the plate height ℓ_b. The measurements presented in figure 1 are similar to those reported by Grift *et al.* (2019) and Reijtenbagh *et al.* (2023); experimental details are given in § 2.

During the acceleration phase of the motion, the drag force F_D increases steadily, until it reaches a peak value at the end of the acceleration phase. When the acceleration ceases, and the plate assumes a constant velocity V_a, the drag force gradually relaxes to its steady-state value. Five repetitions of the measured drag force are superimposed to illustrate the experimental variation. The black solid lines in figure 1 indicate $F_{QS} + F_{AM}$. The drag force during the acceleration phase of the plate is underestimated, and also, after the acceleration ceases and the plate assumes a constant velocity, the drag force does not suddenly drop to F_{QS}, as would be predicted by F_{AM}, but instead gradually relaxes to the steady state value. Evidently, the experimental results in figure 1 for different combinations of acceleration a and final velocity V_a show that the inviscid added mass force F_{AM} does not properly describe the force during the acceleration and relaxation phases of the motion. The peak in $F_D(t)$ at the initiation of the motion is the result of the engagement of the robot that drives the plate motion, as is explained in Appendix A. Note that when we use t^* for the horizontal axis in figure 1(*e–h*) the measured drag force F_D at the start of the motion is compressed towards $t^* = 0$, as the plate barely moves at the start of the motion.

The objective of this experimental study is to expand the approach of Reijtenbagh *et al.* (2023) to find a scaling law for the drag force on starting plates. We first consider motions where the acceleration is constant as in the study of Reijtenbagh *et al.* (2023). However, in the present work the drag force is considered during the entire motion, rather than only the peak force at the end of the acceleration phase. Also, to test the validity of the model proposed by Reijtenbagh *et al.* (2023) motions are repeated in fluids with different viscosities, and we perform measurements for motions with non-constant acceleration. We first consider a motion where the plate is initially at rest and is subsequently accelerated with a constant jerk $J = \dot{a} = \text{constant}$. This motion avoids a discontinuous change in the acceleration at the start of the motion. Finally, we consider a motion where the plate is accelerated such that the velocity increases with the square root of time, i.e. $V(t) \propto \sqrt{t}$. This motion would predict a constant acceleration drag force $F_a(t)$ according to the model proposed by Reijtenbagh *et al.* (2023).

One of the complications of finding proper scaling laws for the drag force during an accelerating motion is that the velocity of the object changes constantly, while the final velocity V_a at the end of the acceleration phase is yet 'unknown' during the acceleration phase. This implies that we cannot identify a proper characteristic velocity of the motion, and thus also cannot identify a proper velocity-based Reynolds number to characterize the fluid motion. Hence, we look for alternative dimensionless numbers that are invariant to the motion. This is further discussed in § 3.

An outline of this paper is as follows. Section 2 describes the experimental methods that are used to determine the forces on the accelerating plates, including the experimental

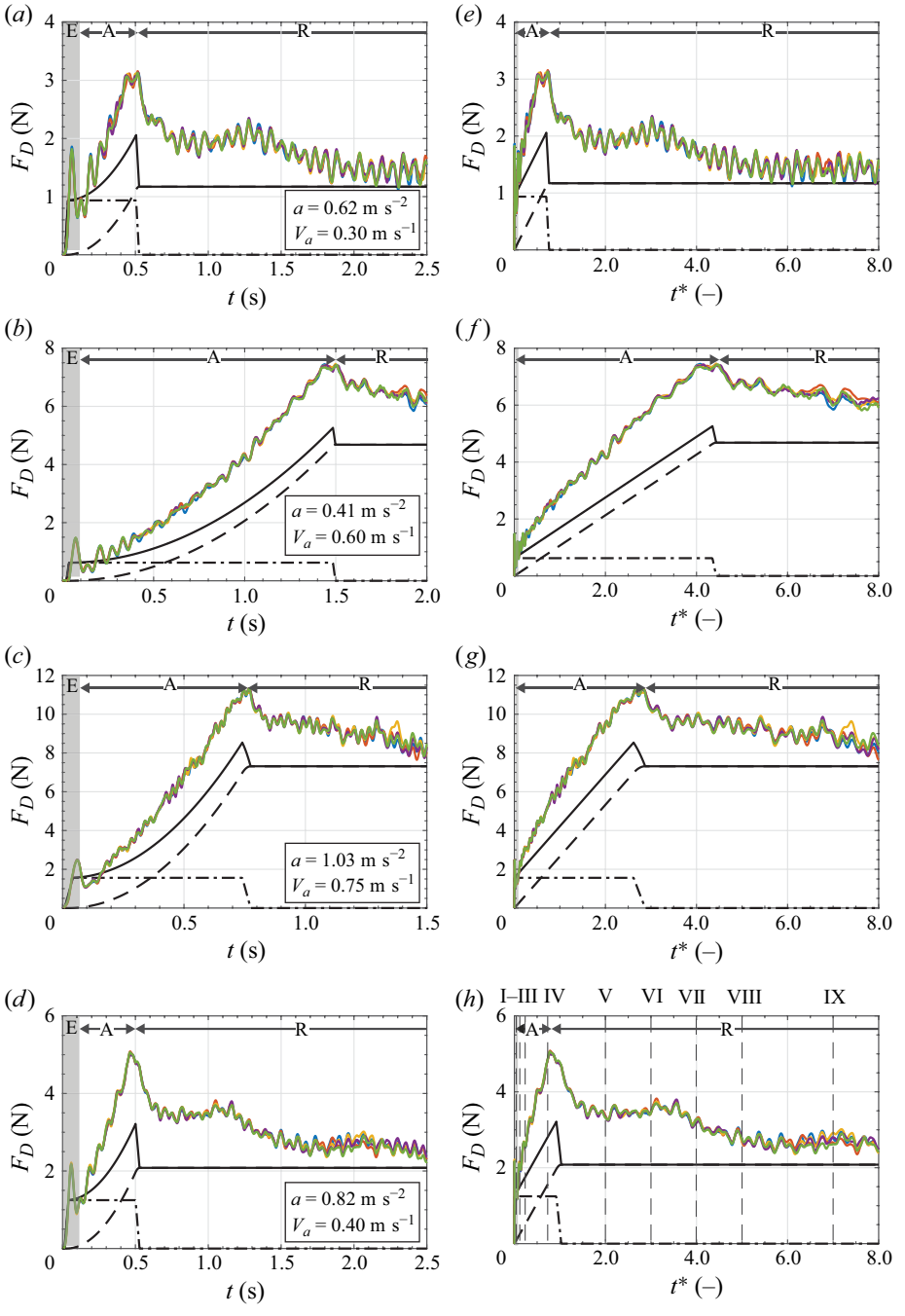

Figure 1. The measured drag force $F_D(t)$ on a rectangular plate with frontal area $A = \ell_a \times \ell_b = 0.2 \times 0.1\,\mathrm{m}^2$ for a motion with constant acceleration a until it reaches a final velocity V_a. Different colours represent the results for five repetitions of the same experiment. Data for four different combinations of the acceleration a and velocity V_a are plotted as a function of (*a–d*) time t in seconds, and (*e–h*) dimensionless time t^*, defined in (1.2). The black lines indicate the quasisteady drag force, $F_{QS} = C_D(1/2)\rho V^2(t)A$ (– – –); the inviscid added mass force, $F_{AM} = m_h a(t)$ (— · —), with m_h given by Payne (1981); the combined force, $F_{QS} + F_{AM}$ (——). The acceleration phase of the motion is indicated by 'A', and the relaxation phase by 'R'. The shaded area labelled 'E' on the left-hand side in each graph indicates the robot engagement at the start of the plate motion, see Appendix A. The roman numerals refer to the flow fields shown in figures 4 and 5.

facility, the different motions, the geometries of the plates and the different working fluids, in addition to the methods used to measure the forces and flow field. Section 3 explains the model that describes the acceleration drag force $F_a(t)$ during the acceleration phase and subsequent relaxation phase. Also a modified Reynolds number is identified that does not explicitly depend on the velocity. This acceleration Reynolds number is used to scale the acceleration drag force. Sections 4 and 5 present the results of the experiments for both the constant acceleration and non-constant acceleration motions. The main conclusions of this study are summarized in § 6.

2. Experiments

2.1. *Experimental set-up*

Figure 2 shows the experimental set-up, which is identical to that of Grift *et al.* (2019). It consists of a rectangular plate with an aspect ratio of 1 : 2 (AR = 2) with a width ℓ_a of 0.200 m, a height ℓ_b of 0.100 m and thickness ℓ_c of 4 mm, connected to an industrial gantry robot (Reis Robotics RL50). The plate is translated through a $2.00 \times 2.00 \times 0.60\,\mathrm{m}^3$ water-filled tank, with a water height of 0.50 m. The top of this plate is $1.5\ell_b$ below the water surface, so that it can be considered fully submerged (Grift *et al.* 2019). With a frontal area of $A = \ell_a \times \ell_b = 0.020\,\mathrm{m}^2$, the blockage ratio is 0.02, which is well below the value of 0.06 for which walls may begin to influence the drag force (West & Apelt 1982). In addition to this rectangular plate, a square plate and a circular plate, both with $A = 200.0\,\mathrm{cm}^2$, are also tested, in addition to AR = 2 rectangular plates with frontal areas of 312.5 and 112.5 cm^2, respectively, see § 4.2. All plates are made of acrylic and have the same thickness, i.e. 4 mm.

The use of thin plates, instead of streamlined bodies, has the advantage that the quasisteady drag coefficient C_D in (1.1) hardly varies with the Reynolds number Re when $Re > 10^3$ (Blevins 2003), see also § 3.1.

In this paper we focus on measurements of the drag force on AR = 2 rectangular plates, following Ringuette, Milano & Gharib (2007), Grift *et al.* (2019) and Reijtenbagh *et al.* (2023). One can argue that it makes more sense to primarily consider a circular plate, and later test for other geometries. There are two main reasons for using the rectangular AR = 2 plate. As shown by Fernando & Rival (2016) and Grift *et al.* (2019), there are clear peaks in the drag force at certain values of t^* that occur due to significant changes in the originally formed vortex ring behind a circular plate. Also, Fernando & Rival (2016) and Fernando *et al.* (2020) show that circular plates show a large decrease of F_D after the acceleration phase until $t^* \approx 20$, even below what is expected from a steady-state drag force. With this in mind, one could question the validity of (1.1) during the relaxation phase of the motion, and even during the acceleration phase. These complications do not appear to occur for rectangular plates, where the drag force F_D during the relaxation phase decays more or less gradually to the expected steady-state value, see figure 1.

The robot is programmed to move the plates through the fluid along a straight path in the middle of the tank. The start and end positions of the plate are at least three times the plate height from the front and rear facing tank walls. Previously Grift *et al.* (2019) showed that the flow remains unperturbed over a distance 2.4 times the plate height in front of the plate.

Additional measurements are performed in a smaller tank (with dimensions of $1.50 \times 0.75 \times 0.60\,\mathrm{m}^3$) for three different water–glycerol mixtures to investigate the effect of the fluid viscosity ν, see table 1. The smaller tank is designed such that the plates can reach a final velocity V_a of $0.90\,\mathrm{m\,s}^{-1}$ for a large range of accelerations without any wall effects by keeping the blockage ratio of the rectangular plate below 0.06. The finite

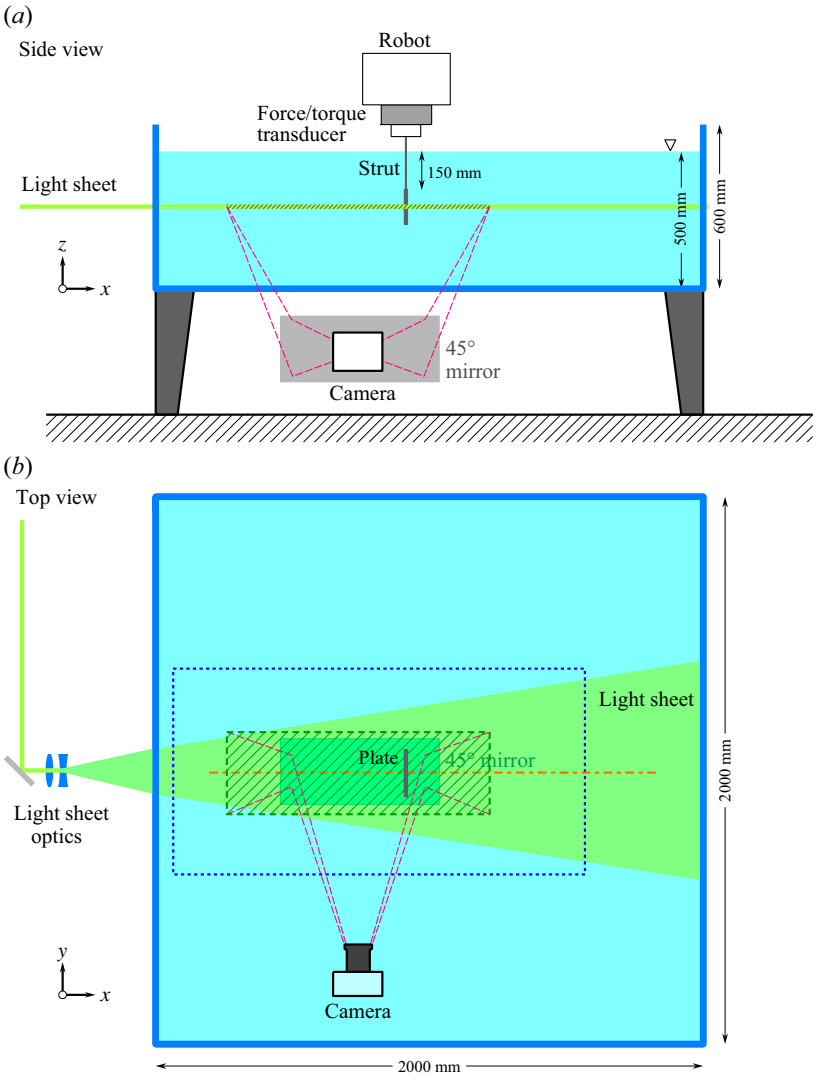

Figure 2. Schematic of the experimental set-up, viewed from the side (*a*) and from above (*b*), consisting of a large water-filled tank, with a gantry robot moving a plate with a prescribed motion. A light sheet illuminates a planar cross-section of the flow through the middle of the plate. A digital high-speed camera is positioned below the water-filled tank and observes the flow through a 45° mirror. The shaded area represents the field-of-view of the camera. For the measurements in the water–glycerol mixtures at elevated viscosities a smaller tank, outlined by the dotted line, is placed inside the larger tank, see text for further details. Photographs of the experimental set-up are available as Supplementary material at https://doi.org/10.1017/jfm.2025.11107.

length of the smaller tank limits the final plate velocity V_a to $0.90\,\mathrm{m\,s^{-1}}$. The full range of experiments with constant accelerations is given by table 2. The motions in experiments with non-constant accelerations are shown in figure 3 and details of these experiments are given in table 3.

The plate is connected to the gantry robot with a streamlined strut. We use either of two force sensors between the robot and the plate, where one sensor (ATI Gamma 32-2.5) is used for measurements with lower final velocities ($V_a < 0.6\,\mathrm{m\,s^{-1}}$), while the other sensor (ATI Delta 660-60) is used for those with higher velocities ($V_a \geqslant 0.6\,\mathrm{m\,s^{-1}}$).

liquid	glycerol [wt %]	glycerol [vol %]	μ [mPa s]	ρ [kg m^{-3}]	ν [mm^2 s^{-1}]
V1 (water)	—	—	0.976	998	0.978
V2	31.64	27.0	2.55	1075	2.37
V3	39.51	34.3	3.52	1095	3.22
V4	46.83	41.4	4.99	1115	4.48

Table 1. The dynamic viscosity μ, density ρ and kinematic viscosity ν of water (V1) and water–glycerol mixtures (V2–4).

		a [m s^{-2}]							Re [10^3]			
		0.41	0.62	0.82	1.03	1.23	1.44	1.64	V1	V2	V3	V4
	0.30	•	•	•	•	•	•	•	30.0	12.7	9.3	6.7
	0.45	•	•	•	•	•	•	•	45.0	19.0	14.0	10.0
	0.60	•	•	•	•	•	•	•	60.0	25.3	18.6	13.4
V_a [m s^{-1}]	0.75	×	•	•	•	•	•	•	75.0	31.6	23.3	16.7
	0.90	×	×	•	•	•	•	•	90.0	38.0	28.0	20.1
	1.05		×	×	×	×	×	×	105.0	—	—	—
	1.20			×	×	×	×	×	120.0	—	—	—
	1.35						×	×	135.0	—	—	—

Table 2. Overview of the accelerations a and final velocities V_a in the constant-acceleration experiments with the AR = 2 rectangular plate. Crosses indicate the combinations of acceleration and velocity that are done with water only; dots indicate the combinations of acceleration and velocity with water and water–glycerol mixtures at higher viscosities. The Reynolds number Re is given by the velocity V_a, the plate height ℓ_b and the kinematic viscosity ν of the fluid, i.e. either water (V1) or the water–glycerol mixtures (V2–V4), see table 1.

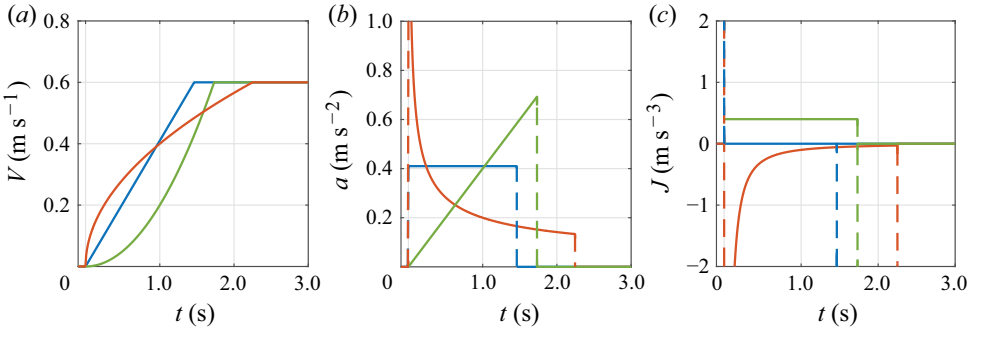

Figure 3. Examples of the programmed plate motions with prescribed (*a*) velocity $V(t)$, (*b*) acceleration $a(t)$ and (*c*) jerk $J(t)$: constant acceleration (blue); quadratic velocity motion (green); square-root velocity motion (red). Dashed lines indicate discontinuities in acceleration or jerk. In this example, the final velocity is $V_a = 0.6$ m s^{-1}, see tables 2 and 3 for an overview of all motions.

The force signals are filtered using a low-pass filter with a 15 Hz cutoff frequency to reduce noise in the measured signal that originates from the robot (Grift *et al.* 2019). The drag force $F_D(t)$ is found from the measured force $F(t)$ by subtracting the inertia $m_p a(t)$ of the plate and the strut, where m_p is their combined mass, and the (very small) measured drag imposed by the strut.

Motion		n	Parameter	Range	V	$a = \dot{V}$	Force F_a
Constant acceleration	$(J = 0)$	1	a [m s^{-2}]	0.10–1.64	at	a	$F_a \propto t^{0.5}$
Quadratic velocity	$(J > 0)$	2	J [m s^{-3}]	0.10–0.80	$(1/2)Jt^2$	Jt	$F_a \propto t^{1.5}$
Square-root velocity	$(J < 0)$	1/2	Q^2 [m^2 s^{-3}]	0.16–0.64	$Q\sqrt{t}$	$(1/2)Q/\sqrt{t}$	$F_a \propto t^0$

Table 3. Overview of three accelerating motions with velocity $V \propto t^n$ and acceleration $a \propto t^{n-1}$, with $n = 1$, 2 and 1/2; these correspond to 'zero jerk' $(J = 0)$, 'positive jerk' $(J > 0)$ and 'negative jerk' $(J < 0)$ motions, respectively. The scaling for the force F_a is according to the model in (3.1) proposed by Reijtenbagh *et al.* (2023).

2.2. *Particle image velocimetry*

Planar particle image velocimetry (PIV) is used to characterize the flow around the plates. A high-speed camera (Phantom VEO 640 L) is used to record 2560 × 1600 pixel images at a rate of 1000 frames per second of small neutrally buoyant fluorescent tracer particles (Cospheric UVPMS-BR-0.995, with 53–63 µm diameter) suspended in the water-filled tank. A 4 mm-thick light sheet from a frequency-doubled Nd:YLF pulsed laser (Litron LDY304-PIV, 527 nm light wavelength) illuminates the tracer particles in a planar cross-section of the tank. The camera and laser sheet are set up to ensure that the field of view is through the centre of the plate in a horizontal plane. This two-dimensional field is representative of the three-dimensional flow around the plate. The field of view has dimensions of 913 × 477 mm^2, which is sufficient to capture the full width of the wake and to follow the plate over a distance of more than six times the plate height (i.e. $t^* > 6$).

The PIV images are analysed using commercial software (Davis 10.2, LaVision GmbH), using a multipass sliding sum-of-correlation method between the nth frame and $(n + 2)$th frame, with 48 × 48-pixel interrogation regions at the initial pass to 24 × 24-pixel windows at the final pass, and with 50 % overlap between adjacent interrogations windows. The final result for the velocity fields has a data spacing of 4.19 mm (i.e. 8.37 mm spatial resolution). The velocities in the final results pass a universal outlier detection test (Westerweel & Scarano 2005), indicating that the results contain at least 99.8 % valid data; rejected interrogation results are replaced by linear interpolation.

3. Model

3.1. *Background*

Our point of departure is Morison's equation (1.1) as modified by Reijtenbagh *et al.* (2023) to describe the drag force on an accelerating plate. The quasisteady force remains unchanged, and instead of the conventional inviscid added mass for the acceleration drag force $F_a(t)$ we use a history-based acceleration drag force. Reijtenbagh *et al.* (2023) showed that this gives a better representation of the total drag force. Figure 4 shows the flow field around the plate at different dimensionless times. Figure 4(*a*) shows the potential flow solution for a moving plate, which resembles the measured flow field at $t^* = 0.05$ in figure 4(*b*). This indicates that at these short times potential flow, and therefore inviscid added mass, remains a good approximation of the flow and drag force on the plate, although evidence of vorticity at the plate edges is visible. However, note that here $t^* = 0.05$ corresponds to a plate displacement of 5 mm that is just slightly larger than the plate thickness (4 mm).

When the plate further progresses during the acceleration the flow starts to separate and a starting vortex loop is created (Grift *et al.* 2019), visible as the vortex pair in figure 4(*c*).

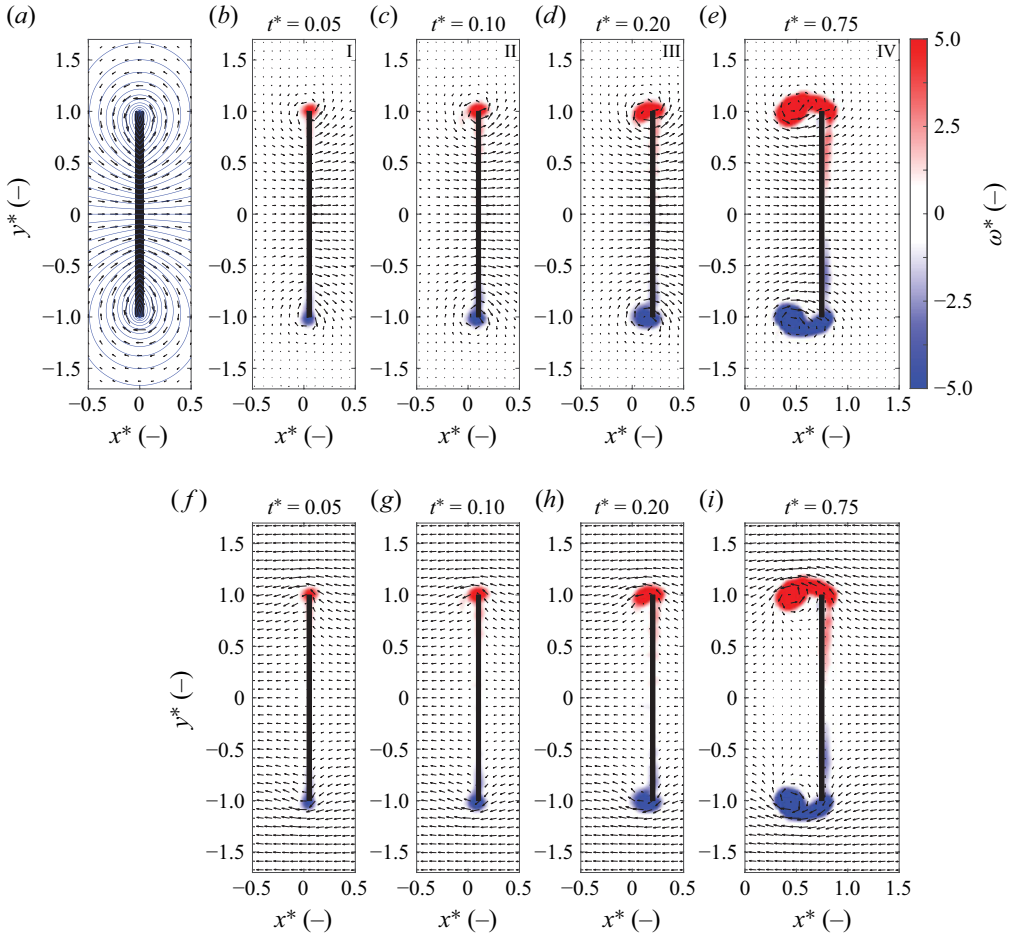

Figure 4. The flow around an accelerating AR = 2 rectangular plate. (*a*) Potential flow around a flat plate, with streamlines in blue. The measured flow around the plate for $a = 0.82\,\mathrm{m\,s^{-2}}$ and $V_a = 0.40\,\mathrm{m\,s^{-1}}$ (corresponding to $Re = 40 \times 10^3$) at dimensionless times: $t^* = 0.05$ (*b*), 0.10 (*c*), 0.20 (*d*) and 0.75 (*e*), respectively, in a fixed frame of reference. The panels (*b–e*) correspond to the roman numerals I–IV in figure 1. Panels (*f–i*) represent the same data as (*b–e*), but now represented in a frame of reference moving with the plate. The colour scale indicates dimensionless out-of-plane component of the vorticity $\omega^* = \omega_z \ell_b / V_a$. Dimensions ($x$, y) are made dimensionless with the plate height ℓ_b. For clarity only one out of four velocity vectors is shown.

Here, potential flow is no longer appropriate to describe the flow, and therefore is not a proper basis for estimating the acceleration drag force $F_a(t)$. This is in line with earlier derivations (Burgers 1921; Biesheuvel & Hagmeijer 2006; Limacher *et al.* 2018) where the acceleration drag force is equal to inviscid added mass at early stages only, without flow separation, and where the vorticity is only present in a thin boundary layer close to the plate. This boundary layer is readily visible in figure 4(*d–e*) (see also figure 18 in Appendix B) and figure 4(*h–i*), where the flow field is represented in a frame of reference that moves with the plate. The incoming flow impinging on the plate resembles a Hiemenz flow (Emanuel 2000), which is that of a stationary irrotational outer flow that resembles a stagnation point flow with a viscous boundary layer with a thickness that is inversely proportional to the square root of the flow Reynolds number. The moving plate in the fluid generates vorticity at the surface that diffuses into the fluid and then advects to the edges

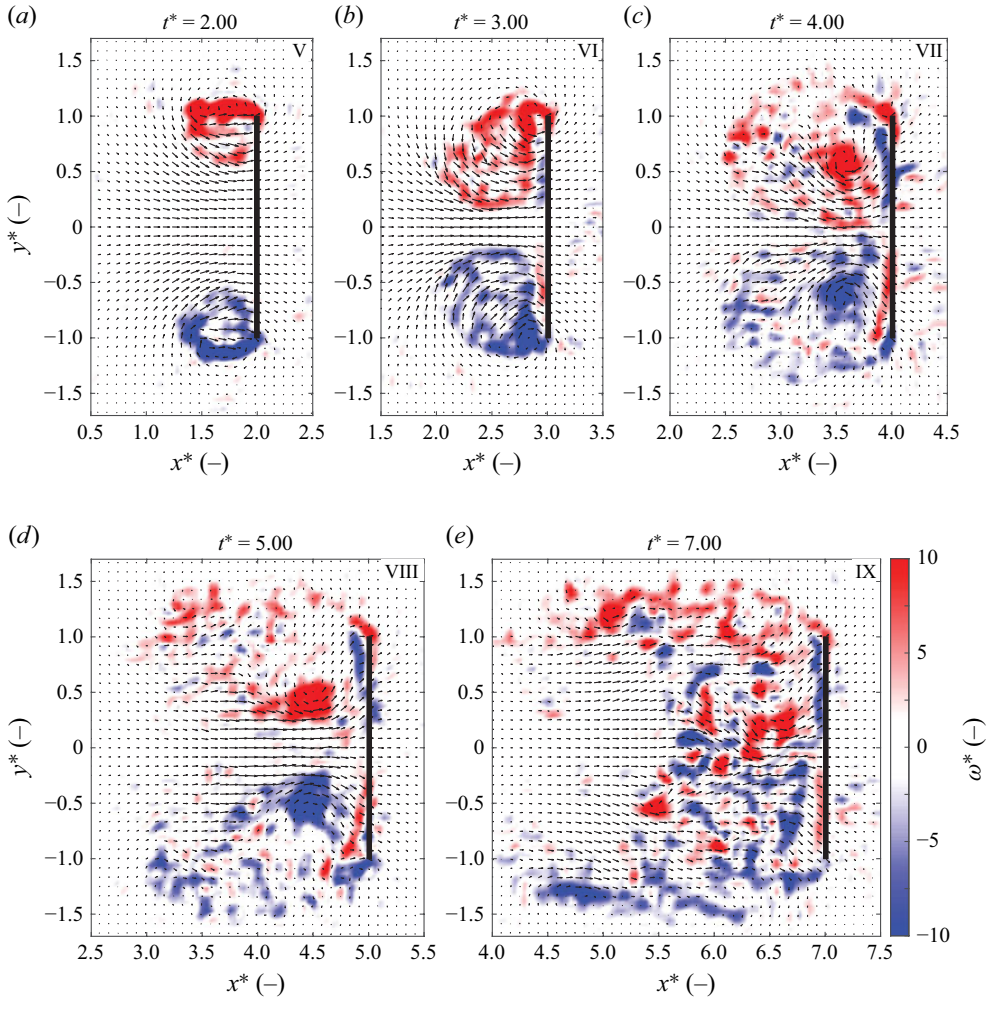

Figure 5. The instantaneous flow field around an accelerating AR = 2 rectangular plate in the same experiment as in figure 4, at dimensionless times $t^* = 2.0$ (*a*), 3.0 (*b*), 4.0 (*c*), 5.0 (*d*) and 7.0 (*e*), respectively. Dimensions (x, y) are made dimensionless with the plate height ℓ_b. For clarity only one out of four velocity vectors is shown. The colours represent the dimensionless out-of-plane component of the vorticity $\omega^* = \omega_z \ell_b / V_a$. The roman numerals correspond to those in figure 1.

of the plate where it accumulates in the vortex (Burgers 1921; Biesheuvel & Hagmeijer 2006). Figure 5 shows the further development of the instantaneous flow to illustrate the transition of the flow into that of a turbulent wake.

Reijtenbagh *et al.* (2023) use Stokes' first problem as an ansatz for a model that incorporates the generation and diffusion of vorticity for an accelerating plate. This is then generalized to account for the advection of vorticity along the plate surface, which leads to a model where the acceleration drag force $F_a(t)$ is proportional to $\sqrt{aV}$. The derivation of this model is summarized in Appendix B.

3.2. *Acceleration drag force*

Combining the results of Xu & Nitsche (2015) and Reijtenbagh *et al.* (2023) we find for the acceleration drag force $F_a(t)$,

$$F_a(t) = \underbrace{C\frac{a^{1/4}\ell^{3/4}}{\nu^{1/2}}}_{C_a}\rho A\sqrt{\nu a V}, \tag{3.1}$$

where C is an empirical constant and ℓ an appropriate length scale. Note that $\sqrt{aV} = at^{1/2}$ for a constant acceleration a. Rewriting (3.1) by eliminating $\sqrt{\nu}$ gives

$$F_a(t) \cong m_h(t)a, \quad \text{with} \quad m_h(t) = \rho A \ell_h(t), \tag{3.2}$$

where $\ell_h(t)$ $(= Ca^{1/4}\ell^{3/4}t^{1/2})$ absorbs the time dependency of (3.1) and other remaining constants, and $m_h(t)$ represents a time-dependent 'hydrodynamic mass' of the accelerating plate (Grift *et al.* 2019). The length scale $\ell_h(t)$ would represent the dimension of the 'volume of fluid' $A\ell_h(t)$ that is thought to be accelerated along with the moving plate (Batchelor 1967). Evidently, the acceleration drag force is not constant, as opposed to the conventional inviscid added mass force obtained from potential flow, which implies $m_h(t)$ grows during acceleration, and (3.2) would represent a generalized approach where the flow can also be rotational. However, the concept of hydrodynamic mass in (3.2) would also imply that $F_a(t)$ vanishes when $a = 0$, which is evidently not the case, see figure 1. Therefore, the association of $F_a(t)$ with a 'hydrodynamic mass' does not seem appropriate in this context.

The dimensionless prefactor C_a in (3.1) is rewritten as

$$C_a = C\frac{a^{1/4}\ell^{3/4}}{\nu^{1/2}} = C\left(\frac{a\ell}{V^2}\right)^{1/4}\frac{V^{1/2}\ell^{1/2}}{\nu^{1/2}} = C\left(a^*\right)^{1/4}Re^{1/2}, \tag{3.3}$$

where $a^* = a\ell/V^2$ is the dimensionless acceleration defined with respect to the velocity V of the moving plate, and Re the Reynolds number defined by the velocity V, the plate dimension ℓ and the kinematic viscosity ν. The constant C is determined experimentally, see § 4.1. It depends on the plate geometry, i.e. AR = 2 rectangular, square or circular plate, but also on the motion; it absorbs the constants C_n, with $n = 1$, 2 and 1/2, that arise from the history-based model explained in Appendix B.

Hence, the acceleration drag force $F_a(t)$ for constant acceleration motion $(n = 1)$, $V(t) = at$; constant jerk motion $(n = 2)$, $V(t) = (1/2)Jt^2$; 'square-root velocity' motion $(n = 1/2)$, $V(t) = Q\sqrt{t}$, given by the history-based model become

$$F_a(t) = C_a\rho A\sqrt{\nu}\begin{cases} at^{1/2} & n = 1, \\ Jt^{3/2} & n = 2, \\ Qt^0 & n = \dfrac{1}{2}. \end{cases} \tag{3.4}$$

When the motions are expressed in terms of t^*, defined in (1.2), we find

$$\begin{cases} at^{1/2} = (t^*)^{1/4}\left(2a^3\ell_b\right)^{1/4} & n = 1, \\ Jt^{3/2} = (t^*)^{1/2}\left(6J\ell_b\right)^{1/2} & n = 2, \\ Qt^0 = (t^*)^0 Q & n = \dfrac{1}{2}. \end{cases} \tag{3.5}$$

Note that for the square-root velocity motion $(n = 1/2)$, $t^* = (2/3)(Q/\ell_b)t^{3/2}$.

3.3. *Acceleration Reynolds number*

The expression in (3.3) can be written as

$$C_a = C\sqrt{Re_a}, \tag{3.6}$$

where Re_a is given by

$$Re_a = \sqrt{a^*}Re. \tag{3.7}$$

This definition of an acceleration Reynolds number Re_a is convenient since it eliminates the velocity V, so what is left is a Reynolds number Re_a that only depends on acceleration. This Reynolds number is equivalent to the acceleration-based Reynolds number introduced by Freymuth, Bank & Palmer (1983) and generalized by Xu & Nitsche (2015) and is equal to the square root of the dimensionless acceleration $\alpha = a\ell^3/\nu^2$ defined by Koumoutsakos & Shiels (1996).

The dimensionless acceleration $a^* = a\ell/V^2$ requires further clarification, especially for the non-constant accelerations of the plate. Our point of departure is the Morison equation, which has two terms: one is the quasisteady drag force F_{QS} and the other one is the acceleration drag force F_a that is due to the acceleration of the surrounding fluid. In the original expression F_a is taken equal to the inviscid added mass force F_{AM} that is associated with potential flow. For a fully submerged AR = 2 rectangular plate, with $A = \ell_a \times \ell_b$, the drag coefficient is $C_D = 1.3$ (Grift *et al.* 2019). For thin plates the drag coefficient C_D is effectively constant over a large range of Reynolds numbers $Re \gg 10^3$ (Hoerner 1965; Blevins 2003). The inviscid added mass force F_{AM} for a rectangular plate is (Brennen 1982)

$$F_{AM} = 0.84\frac{\pi}{4}\rho\ell_a\ell_b^2 a. \tag{3.8}$$

The ratio of the added mass force and the quasisteady drag force, with $C_D = 1.3$, is then

$$\frac{F_{AM}}{F_{QS}} = \frac{0.84\frac{\pi}{4}\rho\ell_a\ell_b^2 a}{1.3 \times \frac{1}{2}\rho V^2\ell_a\ell_b} = \underbrace{\frac{0.84\frac{\pi}{4}}{1.3 \times \frac{1}{2}}}_{1.01}\frac{a\ell_b}{V^2} \cong a^*, \tag{3.9}$$

where ℓ_b is the short dimension of the plate, here referred to as the plate height; the numerical prefactor is close to unity, and therefore ignored here. Hence, the dimensionless acceleration a^* can be interpreted as the ratio of the added mass force relative to the quasisteady drag force.

We can take the same approach for the cases with non-constant accelerations, where both a_n and V_n vary in time (see table 3), such that for $n = 2$

$$a_2 = Jt \quad \text{and} \quad V_2(t) = \frac{1}{2}Jt^2, \tag{3.10}$$

where J is the jerk in [m s^{-3}] and $n = 1/2$ gives

$$a_{1/2}(t) = \frac{1}{2}Qt^{-1/2}, \quad \text{and} \quad V_{1/2}(t) = Qt^{1/2}. \tag{3.11}$$

Substituting (3.10) and (3.11) in the definition for a^* gives

$$a_2^* = \frac{a_2\ell_b}{V_2^2} = \frac{Jt\ell_b}{\frac{1}{4}J^2t^4} = \frac{4\ell_b}{J}\frac{1}{t^3}, \quad \text{and} \quad a_{1/2}^* = \frac{a_{1/2}\ell_b}{V_{1/2}^2} = \frac{\frac{1}{2}Qt^{-1/2}\ell_b}{Q^2t} = \frac{\ell_b}{2Q}\frac{1}{t^{3/2}}, \tag{3.12}$$

respectively. Evidently, the dimensionless accelerations a_2^* and $a_{1/2}^*$ should be independent of time, and therefore only a function of J or Q, the velocity V and the plate height ℓ_b. Substituting V back into the time dependent part from (3.12) for a_2^* and $a_{1/2}^*$ results in

$$a_2^* = \frac{\sqrt{2}\ell_b}{J^{-1/2}} \frac{1}{\frac{1}{2}^{3/2} J^{3/2} t^3} = \frac{\sqrt{2}\ell_b J^{1/2}}{V_J^{3/2}}, \quad \text{and} \quad a_{1/2}^* = \frac{\ell_b Q^2}{2} \frac{1}{Q^3 t^{3/2}} = \frac{\ell_b Q^2}{2V_Q^3}, \tag{3.13}$$

respectively. In addition, it is desirable to maintain a numerator that is proportional to V^2, similar to a^* for constant accelerations, so that in (3.7) the velocity is effectively cancelled in the definition of Re_a while maintaining its scaling with the reciprocal of $\sqrt{\nu}$. To ensure this, a_2^* in (3.13) is raised to the power 4/3 and $a_{1/2}^*$ to the power 2/3,

$$a_2^* = \frac{(4\ell_b^4 J^2)^{1/3}}{V^2}, \quad \text{and} \quad a_{1/2}^* = \frac{\left(\frac{1}{4}\ell_b^2 Q^4\right)^{1/3}}{V^2}. \tag{3.14}$$

Finally, these expressions for a_n^* for non-constant accelerations can be used in (3.7) to find specific Reynolds numbers Re_a^n for the constant jerk motion and 'square-root velocity' motion,

$$Re_a^{n=2} = \frac{(2\ell_b^5 J)^{1/3}}{\nu}, \quad \text{and} \quad Re_a^{n=1/2} = \frac{\left(\frac{1}{2}\ell_b^4 Q^2\right)^{1/3}}{\nu}. \tag{3.15}$$

These expressions for the acceleration Reynolds number Re_a^n are used to determine C_a for different plate motions with different values for Q and J. The acceleration Reynolds numbers Re_a in (3.3) for the constant-acceleration motion and in (3.15) for the constant-jerk and 'square-root velocity' motions, respectively, are each constants during the specified motions. Hence, they can be used for normalizing the acceleration drag forces $F_a(t)$ during each of these motions; this is demonstrated in § 5. They replace the conventional Reynolds number that is defined by the instantaneous velocity, which would constantly change during the motion as the velocity increases during the acceleration phase. In earlier numerical studies of impulsively started plates, i.e. where a plate attains a fixed velocity V_a for $t > 0$, the velocity-based Reynolds number is used to characterize the flow. In this case the plate velocity is increased discontinuously, and the plate does not experience an acceleration phase. This motion is not physical, and in reality any plate that starts to move from rest towards a certain final velocity V_a must experience a finite-duration acceleration phase where the velocity of the plate remains continuous.

4. Constant-acceleration motion

4.1. *Acceleration phase*

The numerical value of the proportionality constant C in (3.1), and consequently C_a in (3.3), is found by a least-squares fit of the model to the measured acceleration drag force $F_a(t) = F_D(t) - F_{QS}(t)$ during the acceleration phase for all measurements in table 2. Figure 6 compares the model with the corresponding fit of $C_a = CRe_a^{1/2}$ in (3.1) with the measured acceleration drag force $F_a(t)$ during a constant-acceleration motion with acceleration $a = 1.03\ \mathrm{m\,s^{-2}}$ and final velocity $V_a = 0.75\ \mathrm{m\,s^{-1}}$. Figure 6 shows that the force $F_a(t)$ grows proportional to $t^{1/2}$, or equivalently $(t^*)^{1/4}$, see (3.5). Evidently $F_a(t)$ exceeds the (constant) inviscid added mass force F_{AM}. Note that F_a at $t^* = 0$ increases almost discontinuously to the value of F_{AM}. This implies that no distinction can be made between the inviscid added mass F_{AM} and the history-based model for $F_a(t)$ at the start of the motion.

When the acceleration ceases and the plate assumes a constant velocity, there is an apparent sharp drop ΔF in F_a. The magnitude of this drop is also predicted by the model, but is not included in the fitting of the model. This is further discussed in § 4.3.

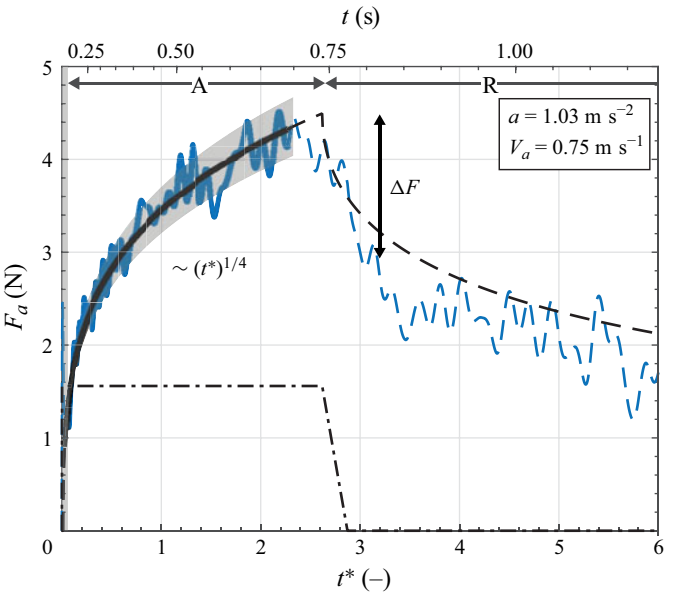

Figure 6. The measured acceleration drag force $F_a(t) = F_D(t) - F_{QS}(t)$ as a function of the dimensionless time t^*, defined in (1.2), during a constant-acceleration motion of an AR = 2 rectangular plate (blue line) with acceleration $a = 1.03\,\mathrm{m\,s^{-2}}$ until the plate reaches a final velocity $V_a = 0.75\,\mathrm{m\,s^{-1}}$. Here $F_a(t)$ is proportional to $(t^*)^{1/4}$, see (3.5). The data highlighted in the bold section is used for fitting the model (3.1), represented by the solid black line, to determine the constant C in (3.3). The dashed black line represents the model in (B8) for $F_a(t)$ during the relaxation phase 'R' after the acceleration ceases, where it drops with a magnitude ΔF, see § 4.3. The dash–dotted line represents the inviscid added mass force F_{AM} given by Payne (1981). The top axis indicates corresponding dimensional time t; note that this is a nonlinear axis. The grey area corresponds to the variation in acceleration during the motion, as indicated in figure 17 of Appendix A.

The resulting values of C_a defined according to (3.3) for accelerations a between 0.41 and $1.64\,\mathrm{m\,s^{-2}}$ and final velocities V_a between 0.30 and $1.35\,\mathrm{m\,s^{-1}}$ are shown in figure 7. The curves in the graph represent C_a in (3.3), with $C = 1.5$ for different values of the Reynolds number $Re = V_a \ell_b/\nu$, where V_a is the final plate velocity at the end of the acceleration phase. This result supports the scaling of $C_a \propto (a^*)^{1/4}$; this rather weak dependence results in a nearly constant value for C_a for the measurements represented in figure 7. These results replace the results previously presented by Reijtenbagh *et al.* (2023), where C_a was considered to be constant for the range of Reynolds numbers Re and values of the dimensionless acceleration a^* for the $200 \times 100\,\mathrm{mm^2}$ rectangular plate and different constants C_a for circular and square plates. The values for C in C_a for different geometries are described in § 4.2.

The acceleration drag coefficient $C_a = C(a^*)^{1/4} Re^{1/2}$ in (3.1) requires further justification. Given the no-slip boundary condition on the plate, which effectively results in the production of vorticity at the plate surface, involves the finite viscosity of the fluid. Reijtenbagh *et al.* (2023) present C_a as a constant that depends on the plate geometry, and is interpreted as a 'Nusselt number' for the advective transport of vorticity over the diffusive transport. Hence, a factor $\sqrt{\nu}$ appears in their expression for F_a, but this serves to dimensionally balance the equation; evidently, a factor $1/\sqrt{\nu}$ should be included in C_a, as in (3.1), to account for the effect of the flow Reynolds number in the 'Nusselt number' for the ratio of advective transport over diffusive transport, see also Appendix B. To investigate this we also conduct measurements in a smaller tank (with dimensions of

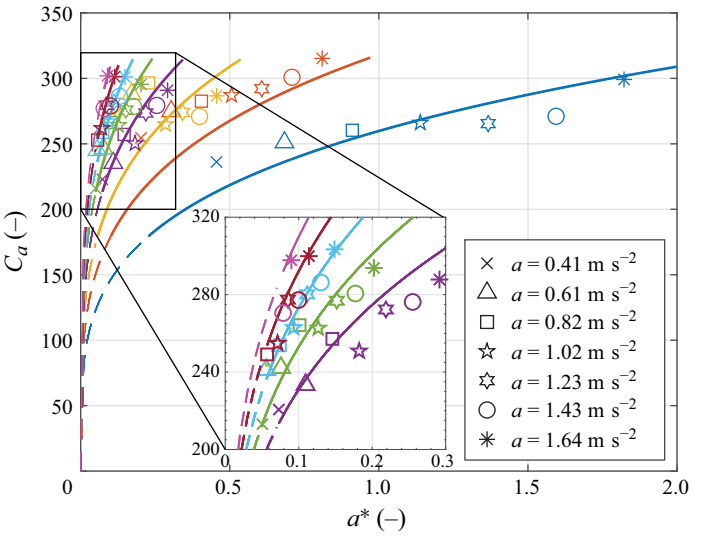

Figure 7. Acceleration drag coefficient C_a as a function of the dimensionless acceleration $a^* = a\ell_b/V_a^2$, where a is the acceleration, ℓ_b the plate height and V_a the final velocity at the end of the acceleration phase. The symbols represent the values of C_a determined experimentally for an AR = 2 rectangular plate with a constant-acceleration motion with acceleration a. The curves represent C_a according to (3.3) at constant Reynolds number $Re = V_a\ell_b/\nu$, where ν is the kinematic viscosity. The colours represent $V_a = 0.30$ (blue), 0.45 (orange), 0.60 (yellow), 0.75 (purple), 0.90 (green), 1.05 (cyan), 1.20 (maroon) and 1.35 m s^{-1} (lilac), respectively.

$1.50 \times 0.75 \times 0.60\,\mathrm{m}^3$) filled with different water–glycerol mixtures that is placed inside the larger tank, see figure 2.

The properties of the different mixtures are shown in table 1. The water–glycerol mixtures are prepared such that the kinematic viscosity is approximately 2, 3 and 4 times that of water. The resulting values for the measured acceleration drag coefficients C_a for the fluid viscosities in table 1 are shown in figure 8(a), where the acceleration drag coefficient C_a is plotted as a function of the Reynolds number $Re = V_a\ell_b/\nu$. This shows that the value of C_a, when considering the data for a single fluid with constant kinematic viscosity ν, remains constant over a considerable range of Reynolds numbers. Note that the values of C_a are elevated as the acceleration a increases, corresponding to its expected scaling proportional to $(a^*)^{1/4}$. When considering fluids with increasing kinematic viscosity ν, the values of C_a drop in proportion to the increase in ν, but remain more or less constant as a function of Re. For the same value of the Reynolds number, $Re = V_a\ell_b/\nu$, the value of C_a depends only on the value of ν; this is in agreement with Hiemenz flow (Emanuel 2000), where the thickness of the boundary layer, for constant approaching velocity and constant length scale, only depends on the value of ν. While it is tempting to fit a line in the graph of figure 8(a) that follows $C_a \propto Re^{1/2}$, this does not lead to the correct scaling of C_a. The data points in figure 8(a) are modified by $Ca^{1/4}\ell_b^{3/4}$ in figure 8(b), with $C = 1.5$, to adjust for the variation in C_a due to acceleration. The variation in C_a is greatly reduced and matches very well with $1/\sqrt{\nu}$. It is noted that the data points in both figures 8(a) and 8(b) for each viscosity appear to display a similar systematic variation; we attribute this to the fact that two different force sensors are used in the measurement (see § 2.1) that have different measurement ranges and accuracy.

Figure 9 summarizes all measurements of C_a as a function of the acceleration Reynolds number $Re_a = \sqrt{a^*}Re$, defined in (3.6). The shaded area indicates the variation in C_a throughout the range of measurements. The data appear to follow a curve $C_a = C\sqrt{Re_a}$,

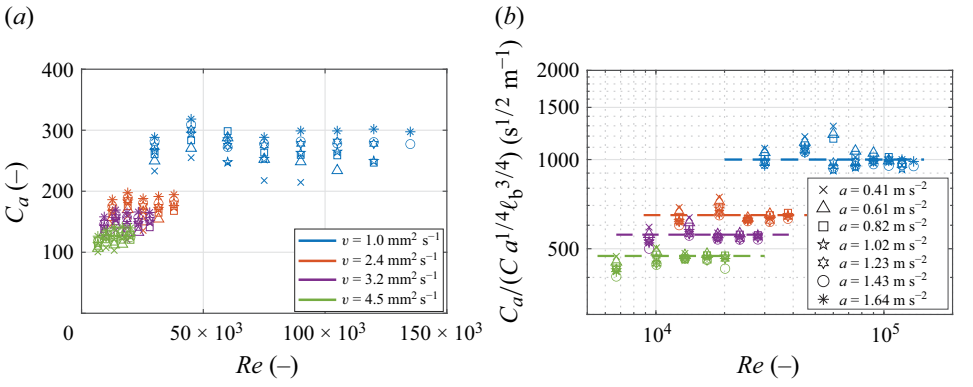

Figure 8. (*a*) The measured acceleration drag coefficient C_a as a function of the Reynolds number $Re = V_a\ell_b/\nu$, where V_a is the final velocity at the end of the acceleration phase, for different accelerations a. The colours indicate four different fluid kinematic viscosities: $\nu = 1.0$ (blue), 2.4 (orange), 3.2 (purple) and 4.5 mm^2 s^{-1} (green), see table 1. (*b*) The same data now represented as $C_a/[Ca^{1/4}\ell_b^{3/4}]$, cf. (3.3), compared with $1/\sqrt{\nu}$, represented by the dashed lines.

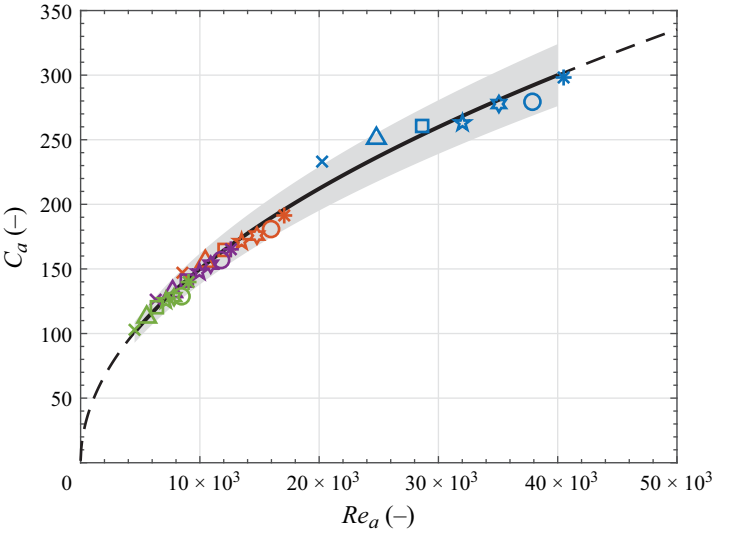

Figure 9. The acceleration drag coefficient C_a as a function of the acceleration Reynolds number $Re_a = \sqrt{a^*}\,Re$ for four different kinematic viscosities, indicated by different colours, as in figure 8. Symbols indicate the median value of results with different final velocities V_a and equal dimensionless acceleration a^* and Re_a, see figure 8. The black line represents $C_a = C\sqrt{Re_a}$, with $C = 1.50\pm0.12$ for an AR = 2 rectangular plate; the shaded region represents the variation of the empirical constant C.

with $C = 1.50\pm0.12$ for the AR = 2 rectangular plate. In § 4.2 it is described how the proportionality constant C varies with plate geometry.

4.2. *Plate geometry*

In the previous section the drag force is considered for an AR = 2 rectangular plate, in correspondence to the plates used in earlier works (Ringuette *et al.* 2007; Grift *et al.* 2019; Reijtenbagh *et al.* 2023). To validate the generality of the developed model and scaling behaviour, we also consider a circular plate, a square plate and AR = 2 rectangular plates

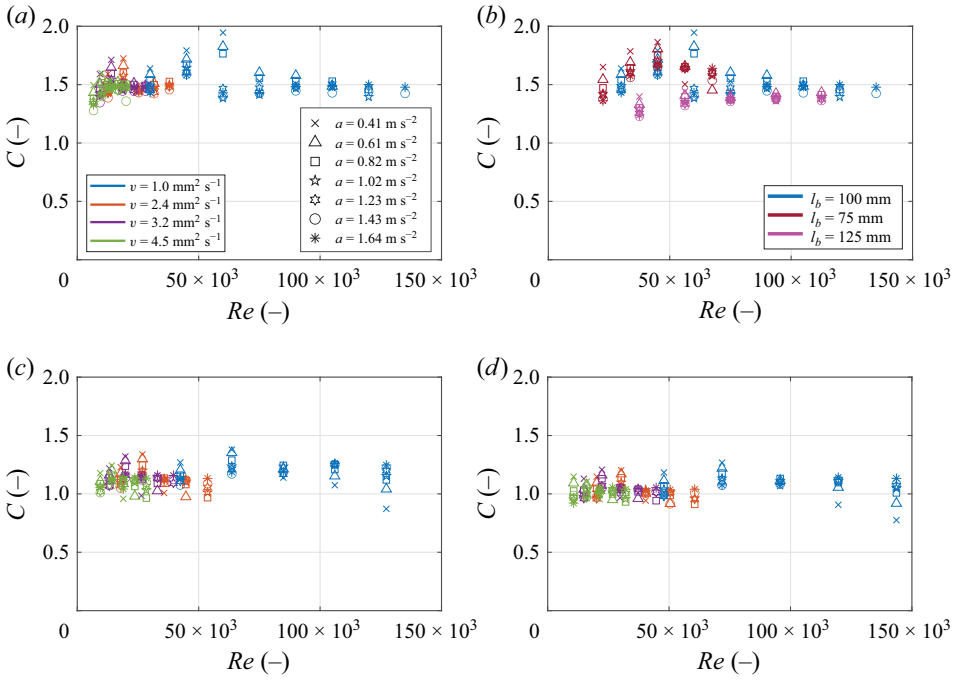

Figure 10. The empirical constant C in (3.1) as a function of the Reynolds number $Re = V_a \ell_b / \nu$, where V_a is the final velocity at the end of the acceleration phase, defined in (3.7), for different sets of parameters: (*a*) C for a $200 \times 100\,\mathrm{mm}^2$ rectangular plate at four different viscosities; (*b*) C for different AR = 2 rectangular plates with different dimensions in water; (*c*) C for a $141.4 \times 141.4\,\mathrm{mm}^2$ square plate at four different fluid viscosities; (*d*) C for a circular plate with a diameter of 159.6 mm at four different viscosities.

with varying dimensions. The circular and square plates both have a frontal area that is equal to that of the rectangular plate, i.e. $A = 200.0\,\mathrm{cm}^2$. In addition, we test AR = 2 rectangular plates with frontal areas A of $25.0 \times 12.5\,\mathrm{cm}^2$ and $15.0 \times 7.5\,\mathrm{cm}^2$.

For each measurement the empirical coefficient C is determined by fitting the model in (3.1) to the measured acceleration drag force $F_a(t) = F_D(t) - F_{QS}(t)$ during the acceleration phase of the motion, see figure 6. The results are summarized in figure 10. All results for the AR = 2 rectangular plate with $A = 200.0\,\mathrm{cm}^2$ for four different fluid viscosities are plotted in figure 10(*a*), which correspond to the data in figure 8. This shows that $C = 1.50 \pm 0.12$. Figure 10(*b*) shows the variation in C for AR = 2 rectangular plates with different dimensions. The same value of $C \cong 1.5$ is found for all three dimensions of the AR = 2 plates. There appears to be a slight systematic variation in C with the plate dimensions, which may be attributed to the ratio of the plate thickness over plate height that is not identical as all plates have the same thickness. Also, the results are affected by using two different force sensors, see § 2.

Figures 10(*c*) and 10(*d*) show the results for C for the square and circular plate, respectively, using the side length and plate diameter as the characteristic length to determine Re_a for the square and circular plate, respectively. Similar to the rectangular plate, C seems to be constant for Reynolds numbers between 10×10^3 and 150×10^3. For the circular plate we find $C \cong 1.04$, and for the rectangular plate $C \cong 1.14$. The ratios of C for rectangular, circular and square plates, i.e. 1.50 : 1.04 : 1.14, are remarkably similar to the ratios of the steady-state drag coefficients C_D at high Reynolds numbers for these plates: 1.30 : 1.14 : 1.25 (Blevins 2003; Grift *et al.* 2019).

4.3. *Relaxation phase*

After the acceleration phase ceases (at time $t_a = V_a/a$) the acceleration drag force $F_a(t)$ drops sharply. This is shown in figure 1 as F_D decays towards a constant force F_{QS} and in figure 6 as F_a decays towards zero. This drop, indicated as ΔF in figure 6, appears to be comparable to F_{AM} in magnitude, and it is tempting to consider the drop in the drag force to be caused by the vanishing of F_{AM} when the acceleration ceases, i.e. $\Delta F = -F_{AM}$. However, the change in the flow field between the moment when the plate still accelerates and when it has assumed a constant velocity is not irrotational. As a matter of fact, vorticity maintains to be created at the surface of the plate and the vortex loop at the plate edge continues to accumulate circulation, albeit at a lower rate, see Reijtenbagh *et al.* (2023, figure 4)

The history-based model described in Appendix B predicts a drop in the force $F_a(t)$ that is proportional to $(t - t_a)^{-1/2}$, see (B8). Indeed, this also implies a sharp drop in $F_a(t)$ at $t = t_a$, and the force $F_a(t)$ initially appears to follow the model, see figure 6. This $t^{-1/2}$ decay is in line with an early theoretical result for the history force on spherical particles at low Reynolds number (Odar & Hamilton 1964). However, later investigations (Mei & Adrian 1992; Lovalenti & Brady 1993) on spherical particles starting from rest showed that for small Reynolds numbers the decay of the history force does not scale as $t^{-1/2}$, but rather as t^{-2}. This is in line with the findings of Grift *et al.* (2019) for the drag force on a plate at high Reynolds number during the relaxation phase.

For longer dimensionless times in the relaxation phase, other effects, such as the detachment and disintegration of the vortex loop, and subsequent transition to a turbulent wake and shedding of vorticity, determine the actual relaxation of the drag force. This typically occurs for dimensionless times $t^* > 4$ (Grift *et al.* 2019).

5. Motions with non-constant acceleration

The previous sections describe the model for the drag force for a constant-acceleration motion. In this section we describe the measurements where the acceleration is either increasing or decreasing in time. We consider two different motions: one with an increasing acceleration ($a = Jt$) where the velocity increases as $V \propto t^2$ with a constant positive jerk $J > 0$, which we name the quadratic velocity motion. Next, we consider the case with a decreasing acceleration, where the velocity increases as $V \propto t^{1/2}$, i.e. with negative jerk $J < 0$, which is referred to as the square-root velocity motion. Further details on these motions with non-constant accelerations are given in table 3 and figure 3.

5.1. *Velocity relation $V \propto t^2$*

We consider a plate that is started from rest and is then accelerated with a constant jerk J, so that the acceleration increases linearly with time, i.e. $a = Jt$, and the velocity increases quadratically with time, i.e. $V = (1/2)Jt^2$.

An example of the measured drag force $F_D(t)$ is shown in figure 11. The measured force is compared with the quasisteady drag force $F_{QS}(t)$, which is now proportional to t^4, and the inviscid added mass force F_{AM}, which is now directly proportional to t; in figure 11, F_{AM} doubles in magnitude from $t = 0.7$ s to 1.4 s. As for the constant-acceleration motion, it is evident that the total drag force during the acceleration phase is higher than the sum of $F_{QS}+F_{AM}$. Instead, the sum of the quasisteady force $F_{QS}(t)$ and the history-based model for the acceleration drag force $F_a(t)$ gives a proper description of the drag force during the acceleration phase, where $F_a(t)$ is given by (3.4), i.e.

$$F_a(t) = C_a \rho A \sqrt{\nu} t^{3/2}, \quad \text{with} \quad C_a = C\sqrt{Re_a}, \tag{5.1}$$

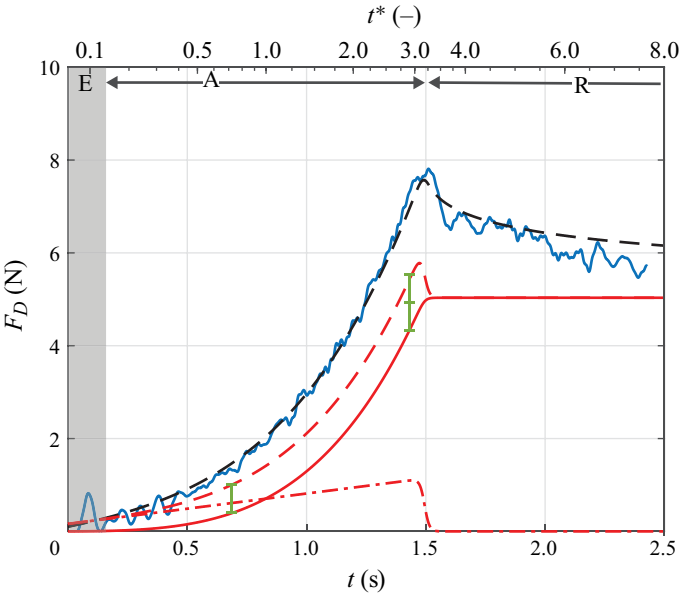

Figure 11. Example of the measured drag force $F_D(t)$ (blue solid line) as a function of time t for a motion with constant jerk $J = 0.4\,\mathrm{m\,s^{-3}}$ until a final velocity $V_a = 0.6\,\mathrm{m\,s^{-1}}$ is reached. The red solid line represents the quasisteady drag force $F_{QS} = C_D(1/2)\rho V^2(t)A$; the red dash–dotted line represents the inviscid added mass force $F_{AM} = m_h a(t)$ that follows from potential flow; the red dashed line is the sum $F_{QS} + F_{AM}$. The black dashed line is the sum $F_{QS} + F_a$, where $F_a(t)$ is the model for the acceleration drag force in (3.4) during the acceleration phase; the relaxation phase is determined numerically as described in Appendix B. The top axis indicates the dimensionless time t^*, equivalent to the number of plate heights ℓ_b travelled by the plate. The acceleration phase is indicated by 'A', and the relaxation phase with 'R' ; the shaded region ('E') indicates the engagement phase of the robot. The vertical green bars indicate where the inviscid added mass F_{AM} has doubled in magnitude.

where $Re_a = Re_a^{n=2}$ is the acceleration Reynolds number, defined in (3.15). We note that the empirical constant C has a numerical value $C = 1.5(C_2/C_1) \approx 1.0$, see Appendix B.

This motion provides a smoother start that avoids large discontinuities in velocity and acceleration. It mitigates the initial peak in the measured force due to the robot engagement (see Appendix A), although the effects of robot engagement and a small jump in acceleration at $t = 0$ could not be fully avoided. However, the magnitude of the initial peak in the force signal is considerably smaller compared with those in the measurements with a constant-acceleration motion, cf. figures 1 and 6.

The history-based model also provides a reasonable description of the drag force during the relaxation phase. The decay of $F_a(t)$ during the relaxation phase for the history-based model does not have an analytical expression, and is computed numerically, see Appendix B. Yet, it follows a similar decay as during the relaxation phase for the constant-acceleration motion.

Figure 12(a) shows the result for the measured acceleration drag force $F_a(t) = F_D(t) - F_{QS}(t)$ for values of the jerk J between 0.1 and $0.8\,\mathrm{m\,s^{-3}}$. The measurements are compared with the model prediction for $F_a(t)$. The same measurement data and model predictions are shown in figure 12(b), but now plotted as a function of the dimensionless time t^*. For each value of the jerk J the acceleration drag force F_a grows proportional to $(t^*)^{1/2}$, see (3.5). Note that the initial peak due to the robot engagement, visible in figure 12(a), nearly coincides with the vertical axis $t^* \approx 0$ in figure 12(b), and thus does not appear to make a significant contribution during the plate motion as a whole.

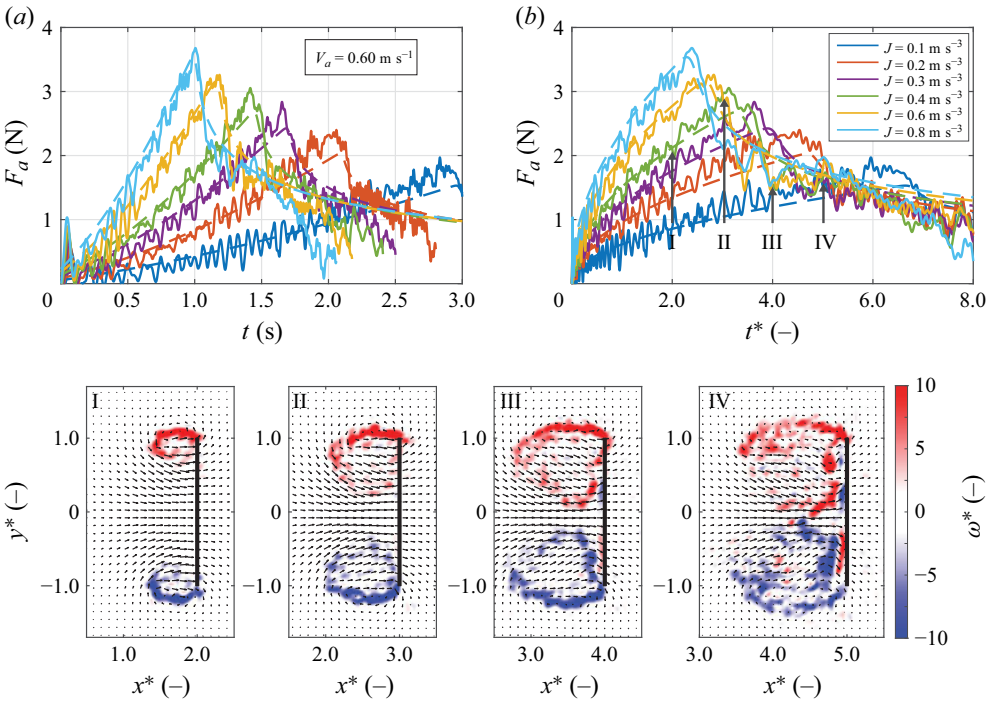

Figure 12. (*a*) The measured acceleration drag force $F_a(t) = F_D(t) - F_{QS}(t)$ as a function of time t for the constant jerk motion of an AR = 2 rectangular plate with acceleration $a = Jt$ for different values of the jerk J between 0.1 and 0.8 m s^{-3}, see table 2. The final velocity is $V_a = 0.60$ m s^{-1} for all measurements. The initial peak is due to the engagement of the robot that moves the plate. The dashed lines correspond to the forces predicted by the model (3.4) with $F_a \propto t^{3/2}$. (*b*) Same data as in (*a*), but presented as a function of the dimensionless time t^*. Below are four PIV snapshots at $t^* = 2.0$ (I), 3.0 (II), 4.0 (III) and 5.0 (IV), respectively, for the motion with $J = 0.4$ m s^{-3}, as indicated by the roman numerals in (*b*). The colour indicates the dimensionless out-of-plane vorticity $\omega^* = \omega_z \ell_b / V_a$.

The agreement between the measured data and the model is remarkably good, taking into consideration the fluctuations in the measured force signals that are the result of the somewhat noisy signal from the force sensor. The prediction is more accurate for short times ($t^* < 4$), where we observe a concentrated vortex loop near the plate edges (see figure 4). For longer times ($t^* > 4$) the vortex loop detaches from the plate and the wake starts to become more complicated, as can be seen in the PIV snapshots indicated by the roman numerals in figure 12. The development of the vortex loop into a turbulent wake is not included in the history-based model.

5.2. *Velocity relation $V \propto \sqrt{t}$*

Here we consider a motion where the velocity $V(t)$ increases with the square root of time, i.e. $V(t) = Qt^{1/2}$. This motion implies that the kinetic energy of the plate increases at a constant rate, i.e. $(1/2)m_P V^2 = (1/2)m_P Q^2 t$, where m_P is the mass of the plate and the strut. Hence, the square of the parameter Q can be interpreted as constant 'power per unit mass' (with a dimension m^2 s^{-3}) added to the plate kinetic energy. For this motion the acceleration a is equal to $a(t) = (1/2)Qt^{-1/2}$, which implies an infinite acceleration at the start of the motion. This is evidently not realistic, and in practice the start of the motion is limited by the finite jerk and maximum acceleration that can be achieved by the robot. For this motion the history-based model predicts an acceleration drag force F_a that is constant, i.e.

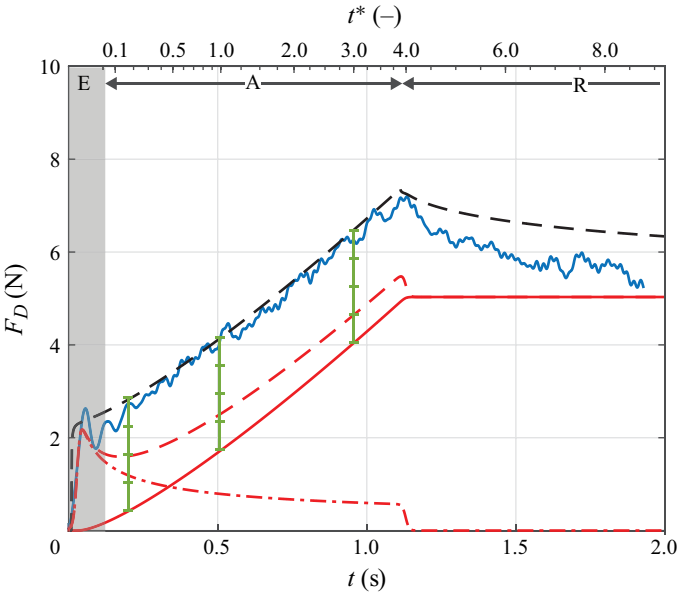

Figure 13. Example of the measured drag force $F_D(t)$ (blue line) as a function of time t for an accelerating motion of an AR = 2 rectangular flat plate with a velocity $V(t) = Qt^{1/2}$ with $Q^2 = 0.36\ \mathrm{m^2\,s^{-3}}$ until the plate reaches a final velocity $V_a = 0.60\ \mathrm{m\,s^{-1}}$. The solid red line represents the quasisteady drag force $F_{QS}(t) = C_D(1/2)\rho V^2(t)A$. Note that F_{QS} is not exactly linear at the start of the motion, which is due to the robot engagement and finite jerk that can be employed. The red dash–dotted line represents the added mass force $F_{AM} = m_h a(t)$ that follows from potential flow; the red dashed line is the combination $F_{QS} + F_{AM}$. The black dashed line is the sum $F_{QS} + F_a$, where $F_a(t)$ is the model for the acceleration drag force in (3.4) according to the actual plate motion, rather than the prescribed motion. The top axis indicates the dimensionless time t^*, equivalent to the number of plate heights ℓ_b travelled by the plate. The acceleration phase is indicated by 'A', and the relaxation phase with 'R' ; the shaded region ('E') indicates the engagement phase of the robot. The vertical green bars indicate where the amplitude of the inviscid added mass F_{AM} has reduced to approximately one half, one third and one quarter in magnitude.

$$F_a \propto \sqrt{aV} = \left(\frac{1}{2}Qt^{-1/2} \times Qt^{1/2}\right)^{1/2} = \frac{1}{\sqrt{2}}Q. \tag{5.2}$$

This implies that during this motion the acceleration drag force $F_a(t)$, given in (3.4), remains constant while the acceleration decreases with time, i.e.

$$F_a(t) = C_a \rho A \sqrt{\nu} Q, \quad \text{with} \quad C_a = C\sqrt{Re_a}, \tag{5.3}$$

where $Re_a = Re_a^{n=1/2}$ is the acceleration Reynolds number defined in (3.15). We note that the empirical constant C has a numerical value $C = 1.5(C_{1/2}/C_1) \approx 1.2$, see Appendix B.

The result that $F_a(t)$ is expected to remain constant, while the magnitude of the acceleration $a(t)$ decreases, is evidently in contrast to the inviscid added mass force F_{AM}. Hence, this can be considered as a critical test for the history-based model to predict the drag force $F_D(t)$, and in particular the contribution of $F_a(t)$.

Figure 13 shows an example of the measured drag force $F_D(t)$. Given that the velocity $V(t)$ increases proportionally to $V \propto t^{1/2}$, the quasisteady drag force F_{QS} increases linearly with time. In this figure it can be seen that this is not exactly the case for the initial part of the motion. This is due to the robot engagement and the finite maximum jerk and acceleration that the robot can achieve. However, it is evident that the measured acceleration drag force $F_a(t) = F_D(t) - F_{QS}(t)$ remains constant in magnitude during the accelerating phase of the motion.

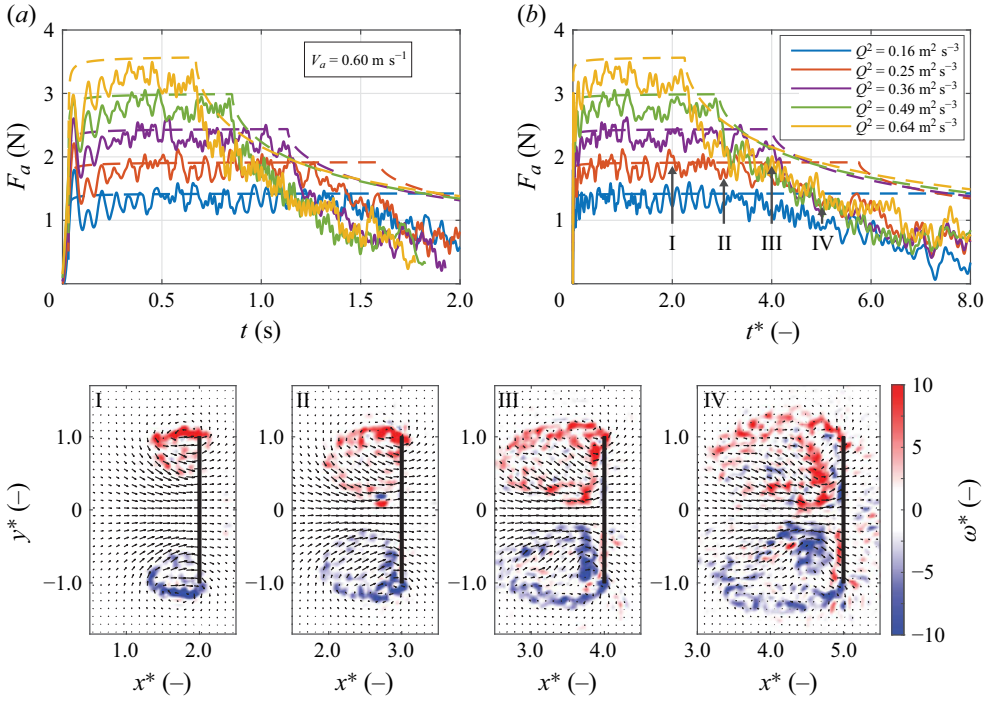

Figure 14. (*a*) The acceleration drag force $F_a(t) = F_D(t) - F_{QS}(t)$ as a function of time t for the motion of an AR = 2 rectangular plate that moves with a velocity $V(t) = Qt^{1/2}$ for different values of Q^2 between 0.16 and 0.64 m^2 s^{-3}, see table 2. The final velocity is $V_a = 0.60$ m s^{-1} for all measurements. The dashed lines correspond to the forces $F_a(t)$ predicted by the model (3.4) with constant $F_a \propto Q$ during the acceleration phase of the motion. (*b*) Same data as in (*a*), but presented as a function of the dimensionless time t^*. Below are four PIV snapshots at $t^* = 2.0$ (I), 3.0 (II), 4.0 (III) and 5.0 (IV), respectively, of the motion with $Q^2 = 0.25$ m^2 s^{-3}, as indicated by the roman numerals in (*b*). The colour indicates the dimensionless out-of-plane vorticity $\omega^* = \omega_z \ell_b / V_a$. Note the deviation between the measured acceleration drag force F_a and the modelled force after $t^* \approx 4$, caused by the detachment and breakup of the vortex loop.

The force $F_a(t)$ during the relaxation phase of this motion is determined numerically (see Appendix B). The predicted values for $F_a(t)$ during the relaxation phase is less accurate, but we note that the motion during the relaxation phase is already beyond $t^* = 4$ (see top axis in figure 13); we already noted that, due to the change in structure of the wake for $t^* > 4$, the history-based model is no longer accurate. We also note that during the robot engagement, i.e. the shaded area adjacent to $t^* = 0$, the magnitude of the drag force $F_D(t)$ is practically equal to that given by the inviscid added mass force F_{AM}, but the same magnitude is given by the numerical result for the history-based model for $F_a(t)$. However, while the inviscid added mass force F_{AM} rapidly drops in accordance with the decreasing magnitude of the acceleration, both the measured drag force and the predicted drag force $F_{QS}(t) + F_a(t)$ closely resemble each other.

Figure 14(*a*) summarizes the results for the measured acceleration drag force $F_a(t) = F_D(t) - F_{QS}(t)$ for values of Q^2 between 0.16 and 0.64 m^2 s^{-3} and with a final velocity of $V_a = 0.60$ m s^{-1} for all measurements. These results further support the model prediction of a constant acceleration drag force F_a. It can be seen that the agreement is not as good for motions with higher values of Q^2. This can be attributed to inaccuracies in the imposed motion due to the mechanical limitations of the robot, see Appendix A. At longer times the measured force $F_a(t)$ drops below the predicted values for the lower

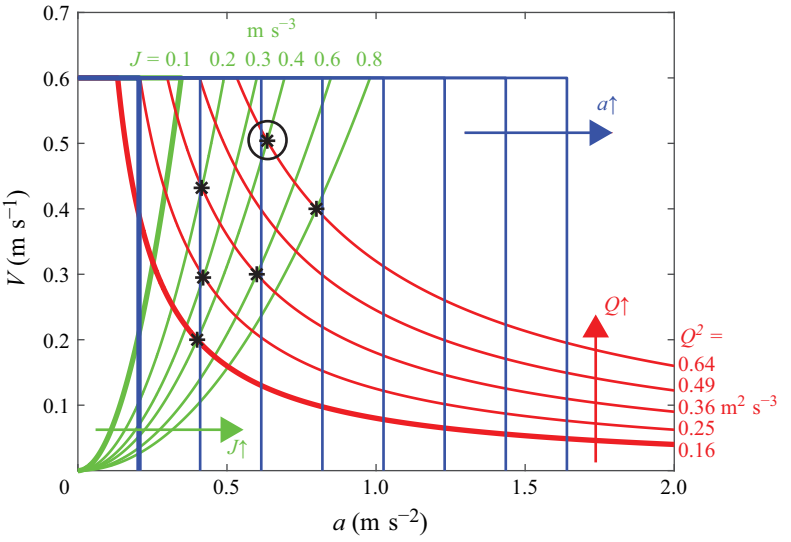

Figure 15. Overview of velocity V and acceleration a for experiments with different motions with a final velocity $V_a = 0.6\ \mathrm{m\ s^{-1}}$. Blue lines show the experiments with constant accelerations, with the acceleration a increasing in the direction of the arrow. Green lines show the experiments with increasing acceleration, with the jerk J increasing in the direction of the arrow. Red lines indicate experiments with decreasing accelerations, with Q^2 increasing in the direction of the arrow. Thick lines indicate the experiments with the lowest value of a, J and Q^2, respectively. Black stars indicate where experiments with all three motion types have (almost) identical values for the velocity and acceleration of the plate. The black circle indicates the identical motion states considered in figure 16.

values of Q^2. When the same data are presented as a function of dimensionless time t^*, as in figure 14(*b*), it shows that the measured force data drop below the theoretical results when the dimensionless time t^* becomes larger than 4, even during the acceleration phase. This can again be associated with the detachment of the vortex loop from the plate edges, the transition to a turbulent wake, and shedding of vorticity from the wake. This is also observed in the experiments of Grift *et al.* (2019), but for a value of $t^* = 6$. The value of $t^* = 4$ where this begins to occur may be attributed to optimal vortex formation (Dabiri 2009).

5.3. *Equivalent motion states*

The two terms in the original Morison equation (1.1) are the quasisteady drag force $F_{QS}(t)$ and an acceleration drag force $F_a(t)$ that is taken equal to the added mass force $F_{AM}(t) = m_h a(t)$, where m_h is the added mass given by the potential flow solution (e.g. Brennen 1982). Note that F_{QS} and F_{AM} only depend on the instantaneous velocity V and acceleration a, respectively. Hence, this suggests that the (total) drag force F_D can be determined without further knowledge of the underlying flow field or the motion history. It is demonstrated in previous sections that the acceleration drag force $F_a(t)$ is not properly described by the inviscid added mass force F_{AM}. Instead, the history-based model (Reijtenbagh *et al.* 2023) in (3.1) implies that the actual acceleration drag force $F_a(t)$ that is added to the quasisteady drag force F_{QS} depends on the flow history. In this section we illustrate this by combining all motions for the AR = 2 rectangular plate considered in this paper, and identify the cases for which the velocity and acceleration are (nearly) equal but were reached by different motions, i.e. different flow (acceleration) histories.

Figure 15 shows all motions considered in this paper, i.e. constant acceleration ($J = 0$), increasing acceleration ($J > 0$) and decreasing acceleration ($J < 0$). Six cases can be

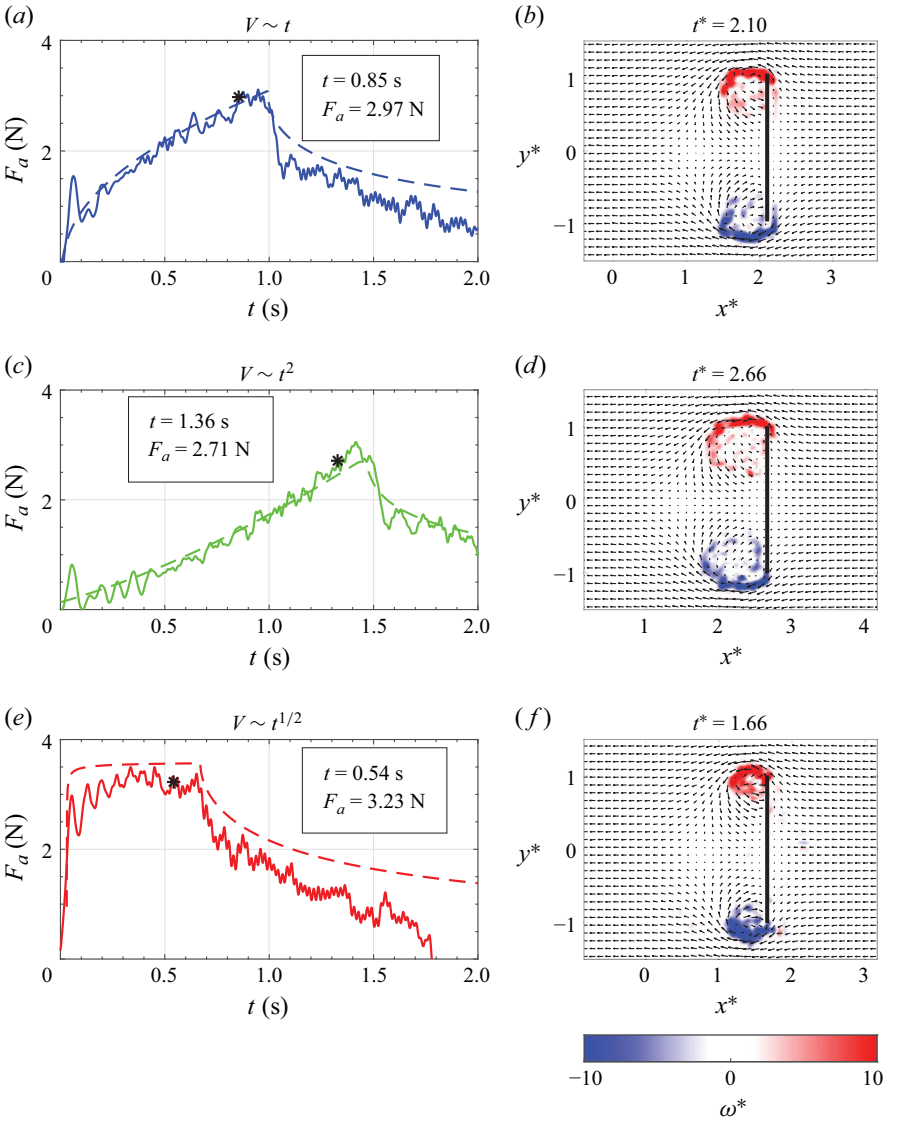

Figure 16. The acceleration drag force $F_a(t)$ as a function of time t and PIV velocity fields for the three different plate motions in table 3, with (*a–b*) constant-acceleration motion with $a = 0.62\,\mathrm{m\,s^{-2}}$; (*c–d*) $V(t) = (1/2)Jt^2$ with $J = 0.40\,\mathrm{m\,s^{-3}}$; and (*e–f*) $V(t) = Qt^{1/2}$ with $Q^2 = 0.49\,\mathrm{m^2\,s^{-3}}$. The $*$ symbols in (*a*), (*c*) and (*e*) indicate the instants when the velocity and the acceleration are equal for all three motions: $a \cong 0.64\,\mathrm{m\,s^{-2}}$ and $V \cong 0.50\,\mathrm{m\,s^{-1}}$, see figure 15. The dashed lines represent $F_a(t)$ according to the history-based model in (3.4) for the acceleration phase, and for the relaxation phase, i.e. (B8) for $n = 1$, and otherwise numerically computed, as described in Appendix B. Panels (*b*), (*d*) and (*f*) show PIV snapshots of the measured velocity field in the midplane of the plate. The colour indicates the dimensionless out-of-plane vorticity $\omega^* = \omega_z \ell_b / V_a$.

identified where instantaneous velocity and acceleration are (almost) equal. However, the acceleration histories are very different between the three different motions. For the case marked by the circle in figure 15, the three measured acceleration drag forces $F_a(t)$ and the three corresponding flow fields are compared in figure 16. Only the force F_a needs to be considered, as the quasisteady drag force $F_{QS}(t)$ is equal for all three cases due to equal instantaneous velocity $V(t)$. The Supplementary material provides a video that visualizes

the PIV flow fields and acceleration drag force $F_a(t)$ simultaneously for the three motions considered here. This case was chosen because the time instants that are compared occur near the end of the acceleration phase of each motion, giving the highest values for $F_a(t)$ and consequently also the largest differences in both the measured drag force and velocity field. In all three cases, velocity and acceleration are equal, i.e. $V = 0.50\,\mathrm{m\,s^{-1}}$ and $a = 0.64\ \mathrm{m\,s^{-2}}$, but the measured acceleration drag forces differ significantly by almost 20 %; the acceleration drag force for the 'square-root motion' (with negative jerk $J < 0$ and $V(t) \propto t^{1/2}$) is the highest in our measurements, while it is the lowest for the 'quadratic motion' (with positive jerk $J > 0$ and $V(t) \propto t^2$), and with the result for the constant-acceleration motion ($J = 0$ and $V(t) \propto t$) between the two.

We note that a significant part of the drag originates from the vorticity in the wake. This vorticity has been created at the plate surface since it was brought into motion from rest. Therefore, the history of the motion needs to be taken into account.

6. Conclusion

This paper describes experimental results for the drag force on accelerating plates. The plates are not only accelerated at a constant rate, i.e. zero jerk ($J \equiv \dot{a} = 0$), but also at non-constant rates of acceleration with either positive jerk ($J > 0$) or negative jerk ($J < 0$). This extends the initial study reported by Reijtenbagh *et al.* (2023), where it was found that the peak acceleration drag force, $F_a(t) = F_D(t) - F_{QS}(t)$, where $F_D(t)$ is the total drag force and $F_{QS}(t) = C_D(1/2)\rho V^2(t)A$ the quasisteady drag force, scales with the square-root of the acceleration for a constant-acceleration motion. This result is in sharp contrast to the inviscid added mass force F_{AM}, which is commonly considered for the acceleration drag force $F_a(t)$ in the Morison equation (Morison *et al.* 1950). Here F_{AM} follows from potential flow theory, and is directly proportional to the plate acceleration. Our experimental results not only show that the acceleration drag force $F_a(t)$ is not constant during a constant-acceleration motion, but also that the actual total drag force can be substantially larger than anticipated when the conventional inviscid added mass force F_{AM} is used for $F_a(t)$.

During the acceleration phase of the motion, the velocity continuously increases. This makes it difficult to define a Reynolds number that is based on the plate velocity. Instead, we define an acceleration Reynolds number Re_a in (3.7) and (3.15) that remains constant during the acceleration phase of each of the motions considered in this paper, which can be used to scale the acceleration drag force F_a. This scaling is tested over a wide range of accelerations, for fluids with different viscosities, and different plate geometries, i.e. rectangular, square and circular plates.

We introduce a model for the acceleration drag force $F_a(t)$ that is based on the concept for the generation of drag for a moving object that was initially proposed by Burgers (1921). The scaling of $F_a(t)$ based on the acceleration, either constant or variable, is reproduced by our model that is based on Stokes' first problem. This is essentially a history term for the imposed velocity, as shown in (B4). The work done by the drag force following the history-based model is validated by comparing this work with the production of kinetic energy in the fluid, as described in Appendix B.2. This describes the work done by the moving plate on the surrounding fluid through the creation of vorticity at the plate surface.

The history-based model predicts the acceleration drag force $F_a(t)$ during the acceleration phase, including a steep, almost step-like, increase of the force at the start of the constant-acceleration motion. At the end of the acceleration phase, when the acceleration ceases, the model also predicts a sharp step-like drop of the drag force, followed by a more gradual decrease of the force during the initial part of relaxation phase

(up to $t^* \approx 4$), see figure 6. Hence, the history-based model can be thought to 'incorporate' the inviscid added mass force. The model requires a semiempirical acceleration drag coefficient C_a that accounts for the advection of the vorticity generated at and diffusing away from the plate surface, and that appears to depend only on the plate geometry. Ideally, C_a should be predicted analytically from a proper theoretical framework, for example an extension to three-dimensional viscous flow of the starting-vortex inviscid theory (Pullin & Sader 2021; Hinton *et al.* 2024; Sader *et al.* 2024).

Similar to constant accelerations, the history-based model provides an accurate prediction of the drag forces at non-constant accelerations. Figure 11 shows an experiment where the plate accelerates from rest with a constant jerk J, which means the acceleration increases linearly in time: $a = Jt$. The conventional prediction with the inviscid added mass force F_{AM} for F_a underestimates the measured drag force, and our proposed history-based model gives a more accurate prediction.

A special case considered here is the motion with $V \propto Qt^{1/2}$, where the history-based model predicts that $F_a(t) = \text{constant}$ during the acceleration phase. This adds to the quasisteady drag force F_{QS} that is proportional to t for $V \propto Qt^{1/2}$. Since the acceleration decreases with time, i.e. $a(t) \propto t^{-1/2}$, any contribution explicitly from F_{AM} would result in a total drag force $F_D(t)$ that is not linear in t. It is evident from the result in figure 13 that this is not the case, suggesting again that the history-based model gives is a better description for $F_a(t)$ in (1.1).

Finally, to underwrite the result that the acceleration drag force $F_a(t)$ depends on the history of the flow, we compare in figure 16 three realizations for a rectangular plate that at a certain instant in three different experiments have the same combination of velocity and acceleration, but with different flow histories. This shows that the original Morison equation, which is based on the instantaneous velocity and the instantaneous acceleration of the object, may not provide a proper prediction for the instantaneous drag force. The present history-based model applies to flat plate geometries; whether this approach is also applicable to other geometries needs further investigation. It should be noted here that the original Morison equation is intended for the variation in velocity for a travelling continuous wave, which is adequately described by potential flow. However, we note that in the case of a periodic motion, the vorticity that is generated during the motion in a forward motion is (partially) cancelled by vorticity of opposite sign in the backward part of the motion, as described in the original paper of Burgers (1921). This is effectively what is described by Stokes' second problem for an oscillating plate. Hence, for a solitary wave or surge, such as in our experiments, the drag force on an object may be substantially larger than predicted by the original Morison equation. Our history-based model for $F_a(t)$ may provide a better estimate.

Supplementary material and movies. Supplementary material and movies are available at https://doi.org/10.1017/jfm.2025.11107.

Acknowledgements. The authors would like to acknowledge the expertise of ing. E. Overmars on PIV, and G. Mulder on the force measurements, as well as the technical support by J. Ruijgrok. We are also grateful to Dr W. van de Water, who brought to our attention the original paper by J.M. Burgers.

Funding. This work is part of the 'ImpulsiveFlows' project that has received funding from the European Research Council (ERC) under the EU Horizon 2020 program (grant no. 884778). Open access funding provided by Delft University of Technology.

Declaration of interests. The authors report no conflict of interest.

Data availability statement. The data that support the findings of this study are available upon request.

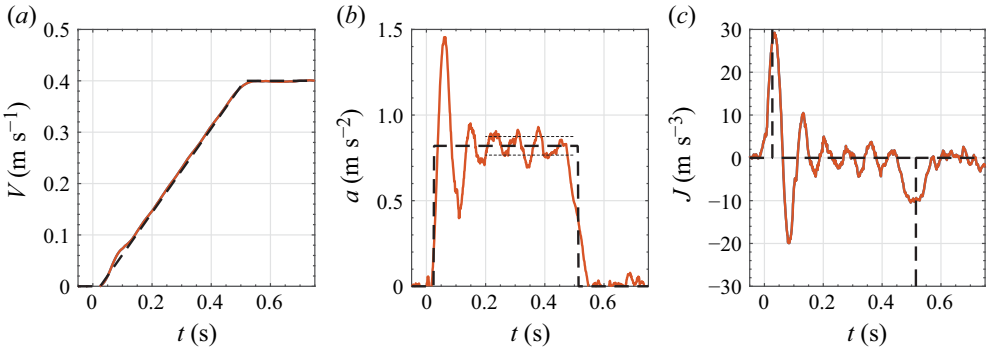

Figure 17. (*a*) The measured velocity $V(t)$, (*b*) acceleration $a(t)$ and (*c*) jerk $J(t)$ for a constant-acceleration motion with $a = 0.82\,\mathrm{m\,s^{-2}}$ and $V_a = 0.40\,\mathrm{m\,s^{-1}}$ in a separate measurement where the robot motion is optically tracked using a target mounted on the strut. The dashed black line is the motion programmed into the robot, while the red line is the actually measured motion. The finite jerk and overshoot in acceleration of the robot system as a result of the robot engagement leads to a difference between the desired and actual motion. The dotted lines in (*b*) represent the root-mean-square variation of the acceleration of $\pm 0.056\,\mathrm{m\,s^{-2}}$, corresponding to variations in the plate velocity of $0.01\,\mathrm{m\,s^{-1}}$.

Appendix A. Robot motion

The robot is programmed to perform different motions with prescribed velocity and acceleration, as shown in tables 2 and 3 and figure 3. The robot can be programmed to impose a motion for a given velocity and acceleration. Hence, it is quite straightforward to programme a motion with constant acceleration. The range of constant accelerations and final velocities used in the experiments is given in table 2. However, for motions that require a varying acceleration the programming is more complicated, and the motion needs to be divided into smaller sections, each with a specified (constant) velocity and (constant) acceleration. The robot has a limited jerk (which cannot be programmed), which smooths out the motion but requires careful programming. When the individual sections are chosen too long, the jerk does not fully smooth out the motion, which results in 'jumps' in its motion; on the other hand, when the individual sections become shorter than the rate at which the robot can respond to the subsequent commands, the robot slows down, leading to erratic motion.

During all experiments, especially for motions that involve a large increase or decrease in acceleration, the robot applies a significant jerk to reach the desired acceleration as quickly as possible. As the robot has a maximum jerk, this is not always possible, and this can lead to small differences between the desired and actual acceleration and velocity of the motion. In addition, the inertia of the robot segments, which also need to be accelerated or decelerated, may cause a deviation between the targeted and actual values of the acceleration. This is commonly experienced in this type of experiments, and such deviations from idealized motions can be observed in measurements reported elsewhere (e.g. Corkery *et al.* 2017; Grift *et al.* 2019; Fernando *et al.* 2020; Galler, Weymouth & Rival 2021; Li *et al.* 2022, 2024; Gehlert *et al.* 2023). In a separate measurement, we measure the actual motion by optically tracking a small target mounted on the strut that holds the plate. An example of the actual motion for the case of constant acceleration is shown in figure 17. This result is exemplary for all measurements presented in tables 2 and 3. It shows that it takes some time for the robot to reach a constant target acceleration and that the acceleration has an overshoot before reaching the target value. This overshoot leads to a peak in the force signals at the start of the motion, referred to as the robot 'engagement'.

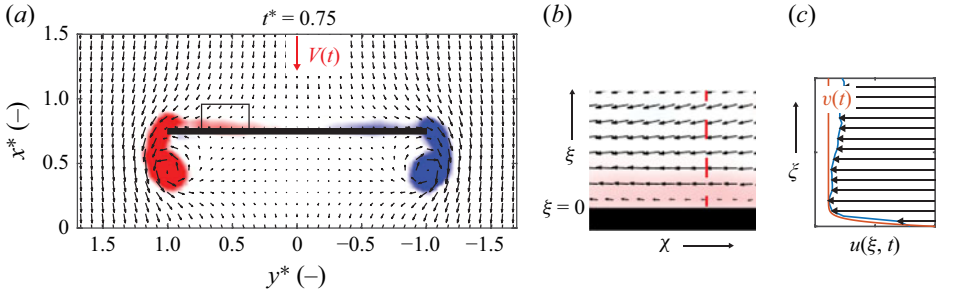

Figure 18. (*a*) Detail of figure 4 for $t^* = 0.75$ in a frame of reference moving with the plate at a velocity $V(t)$. (*b*) Flow in the rectangle of panel (*a*) with coordinates (χ, ξ) parallel and normal to the plate surface, respectively. (*c*) Velocity profile $u(\xi, t)$ at the dashed line in (*b*), compared with the velocity profile in (B5), with $v(t) \propto V(t)$. The colours in (*a*) and (*b*) represent the non-dimensional out-of-plane component of the vorticity ω^*, see figure 4.

The root-mean-square variation of the acceleration of $\pm 0.056\ \mathrm{m\ s^{-2}}$, indicated in figure 17, is representative for all measurements.

Appendix B. History-based model

B.1. *Ansatz*

Following Batchelor (1967), the force for an accelerated object, such as a plate, is attributed to the additional kinetic energy that is needed to also accelerate the surrounding fluid. This implies that work is done by the object on the surrounding fluid. We consider the concept of drag as set out by Burgers (1921), i.e. where the motion of an object in a fluid continuously generates vorticity at the surface of the object. The deformation work on the fluid in contact with the surface of the object represents the work done on the fluid. When we consider a small section of the upstream side of the plate (figure 18), this resembles Stokes' first problem of an impulsively starting plate of infinite length in a semi-infinite space (Batchelor 1967; Schlichting & Gersten 2000). We illustrate this in figure 18. This is essentially a one-dimensional diffusion problem, where the velocity field $u(\xi, t)$ in figure 18 is given by

$$\frac{\partial u}{\partial t} = \nu \frac{\partial^2 u}{\partial \xi^2}, \tag{B1}$$

with initial and boundary conditions

$$\begin{aligned} &t = 0; && \xi > 0; && u(\xi, 0) = v(t = 0), \\ &t > 0; && \xi = 0; && u(0, t) = 0, \\ & && \xi \to \infty; && u(\infty, t) = v(t), \end{aligned} \tag{B2}$$

where $v(t)$ is the velocity of the fluid away from the wall and proportional to the velocity $V(t)$, see figure 18. In the case of an impulsively started flow, i.e. $v(t) = v_a$ for $t > 0$ where v_a is constant, the velocity of the fluid is given by

$$u(\xi, t) = v_a \mathrm{erf}\left(\frac{\xi}{2\sqrt{\nu t}}\right), \tag{B3}$$

where $\mathrm{erf}(z)$ is the error function. Analytical solutions exist for other canonical cases, for example where $v(t)$ is described by a polynomial. When this is not the case, the velocity

$u(\xi, t)$ is given by (Batchelor 1967; Schlichting & Gersten 2000):

$$v(t) - u(\xi, t) = \int_{-\infty}^{t} \frac{\xi}{\sqrt{4\pi\nu}} \frac{v(\tau)}{(t-\tau)^{3/2}} e^{-\frac{\xi^2}{4\nu(t-\tau)}} \mathrm{d}\tau. \tag{B4}$$

This integral also forms the foundation of the Basset history force for spherical particles (see for example Crowe 2012). For an arbitrary motion $v(t)$ for which (B4) has no analytical solution, one can approximate $u(\xi, t)$ numerically. This is not only useful to compute $F_a(t)$ during the relaxation phase for the non-constant acceleration motions, but also can be used to incorporate non-ideal effects in the robot motion, such as the robot engagement due to the finite jerk of the system.

For a linearly accelerating flow with $v(t) = at$ the analytical solution for $u(\xi, t)$ is given by (Crank 1975)

$$v(t) - u(\xi, t) = at \left[\left(1 + \frac{\xi^2}{2\nu t} \right) \mathrm{erfc}\left(\frac{\xi}{2\sqrt{\nu t}} \right) - \frac{\xi}{\sqrt{\pi \nu t}} e^{-\frac{\xi^2}{4\nu t}} \right], \tag{B5}$$

where $\mathrm{erfc}(z) = 1 - \mathrm{erf}(z)$ is the complementary error function. The deformation work done by the plate on the fluid is proportional to the wall shear stress:

$$\tau_w(t) = \rho\nu \left. \frac{\partial u}{\partial \xi} \right|_{\xi=0} = C_1 \rho \sqrt{\nu v(t) a} = C_1 \rho a \sqrt{\nu t}, \tag{B6}$$

with $C_1 = 2/\sqrt{\pi} \cong 1.13$ for a constant-acceleration motion ($n = 1$). This expression is based on the generation and diffusive transport of vorticity in an elementary part of the actual finite size plate in figure 18(*a*). To account for the generation and diffusion over the full plate surface with area A and advection of the vorticity to the edges of the plate, where it accumulates in a vortex loop, we generalize the expression in (B6) to

$$F_a(t) = C_a \rho A \sqrt{\nu V(t) a}. \tag{B7}$$

The semiempirical coefficient C_a is further explained in § 3.2 and can be considered as the geometry-specific momentum equivalent of a Nusselt number. (An equivalent heat transfer problem would be a horizontal plate with a heated bottom surface, where heated air flows along the bottom surface to the plate edges where it forms a vortex loop (see e.g. Al-Arabi & El-Riedy 1976 and Mills & Coimbra 2015).)

Previous experiments (Reijtenbagh *et al.* 2023) on accelerating plates showed that the acceleration drag force $F_a(t) = F_D(t) - F_{QS}(t)$ scales proportional to $a^{0.5}$. Hence, this observation supports the physical description of the force $F_a(t)$ as a history force, based on Stokes' first problem as an ansatz that leads to a scaling proportional to $a^{1/2}$. The corresponding shear stress on the surface of the plate is directly related to the deformation work that acts on the fluid in the vicinity of the plate. The work per unit time is interpreted as done by the 'added mass force' in its most general sense (Batchelor 1967). The inclusion of the viscosity is to match the dimension of the product Va, and is a consequence of the ansatz originating from Stokes' first problem; the actual effect of fluid viscosity is discussed in § 3 and evaluated experimentally in § 4.1.

The previous result applies only to the acceleration phase of the plate, i.e. $t < t_a$. The model is easily extended to represent also the relaxation phase of the plate motion by subtracting the solution (B7) with a time delay t_a to arrive at

$$F_a(t) = C_a \rho A a \sqrt{\nu} \left[\sqrt{t} - H(t - t_a) \sqrt{t - t_a} \right], \tag{B8}$$

where $H(t)$ is the Heaviside step function. This expression not only describes $F_a(t)$ for $0 < t \leqslant t_a$, with $t_a = V_a/a$, but also describes $F_a(t) \propto t^{-1/2}$ for $t \gg t_a$ during the relaxation

phase after the acceleration ceases (Grift *et al.* 2019; Reijtenbagh *et al.* 2023). The model in (B8) is validated in Appendix B.2 for an accelerating circular plate.

For the motions with non-constant accelerations, i.e. $v(t) = (1/2)Jt^2$ (§ 5.1) and $v(t) = Q\sqrt{t}$ (§ 5.2) the above procedure can be followed. Substitution in (B4) yields (Crank 1975, § 3.3)

$$v(t) - u(\xi, t) = 2Jt^2 \left[\left(\frac{1}{4} + \frac{\xi^2}{4\nu t} + \frac{\xi^4}{48\nu^2 t^2} \right) \mathrm{erfc}\left(\frac{\xi}{2\sqrt{\nu t}} \right) - \left(\frac{5\xi}{12\sqrt{\nu t}} + \frac{\xi^3}{24\,(\nu t)^{3/2}} \right) \frac{1}{\sqrt{\pi}} e^{-\frac{\xi^2}{4\nu t}} \right], \tag{B9}$$

and

$$v(t) - u(\xi, t) = Q\sqrt{t} \left[e^{-\frac{\xi^2}{4\nu t}} - \frac{\sqrt{\pi}\xi}{2\sqrt{\nu t}} \mathrm{erfc}\left(\frac{\xi}{2\sqrt{\nu t}} \right) \right], \tag{B10}$$

respectively, which then gives for the wall shear stress τ_w,

$$\tau_w(t) = C_2 \rho J \sqrt{\nu} t^{3/2}, \quad \text{and} \quad \tau_w(t) = C_{1/2} \rho Q \sqrt{\nu}, \tag{B11}$$

with: $C_2 = 4/(3\sqrt{\pi}) = 0.752$, and $C_{1/2} = \sqrt{\pi}/2 = 0.886$. Note that the constants C_1, C_2 and $C_{1/2}$ are $O(1)$ and are absorbed in the generalized acceleration drag force coefficient C.

Generalization of the elementary solutions in (B11), as for (B6)–(B7), then leads to the expressions in (3.4).

B.2. *Validation of the model*

The work done by the drag force on a starting plate is equal to the production of kinetic energy of the fluid motion surrounding the object, while at the early stage of the plate motion the dissipation of kinetic energy remains negligible. This effectively defines the general concept of the added mass force (Batchelor 1967; Brennen 1982).

The conventional approach where the added mass is calculated by means of potential flow does not provide the proper result for the total drag force on an accelerated plate (Grift *et al.* 2019; Reijtenbagh *et al.* 2023). This is also illustrated in figure 19 that shows the work done (blue solid line) on an accelerating circular plate during a motion where the plate is accelerated at a rate of $a = 1.03\,\mathrm{m\,s^{-2}}$ during a period of 0.44 s, until it reaches a velocity of $V_a = 0.45\,\mathrm{m\,s^{-1}}$. This matches the result obtained from a planar PIV measurement of the flow field; during the acceleration phase, and some time after this, the flow field can be considered axisymmetric, so that the total kinetic energy can be found by integrating the measured flow field along the azimuthal direction. This result, shown as the green dashed line in figure 19, matches the directly measured work done on the plate over a substantial distance; the results obtained from the PIV data starts to deviate after termination of the acceleration phase, as the wake becomes unstable and turbulent. Hence, the flow is no longer axisymmetric, and the planar PIV measurement no longer represents the full three-dimensional flow. The work predicted by the sum of the quasisteady drag force $F_{QS}(t) = C_D(1/2)\rho V^2(t)A$, with $C_D = 1.04$ (Blevins 2003) and the inviscid added-mass force $F_{AM}(t) = (1/3)\rho D^3 a(t)$, where D is the plate diameter (Brennen 1982), represented by the black dashed line in figure 19 severely underpredict the actual work done. However, when we consider the drag force, and use the history-based model for $F_a(t)$ in (3.1), as derived in Appendix B, the work done by the plate provides a correct prediction of the measured work for the accelerating plate. This validates the history-based model for $F_a(t)$.

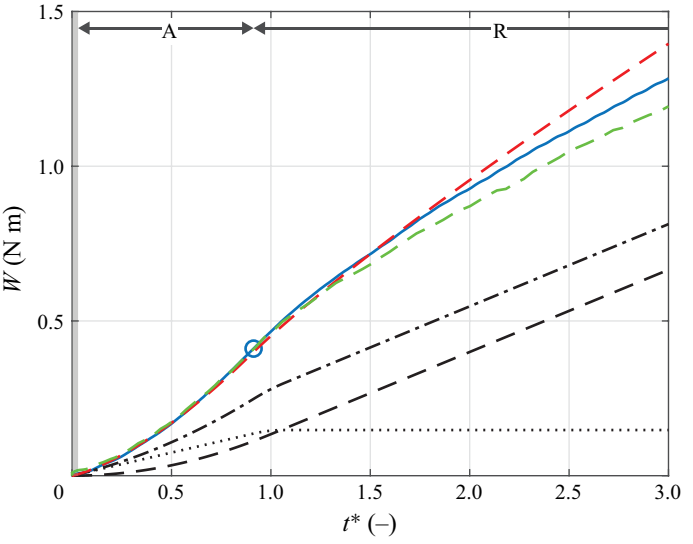

Figure 19. The work $W = \int F_D \ell_b \mathrm{d}t^*$ performed by the drag as a function of dimensionless time t^* for a circular plate that is accelerated at a rate $a = 1.03\,\mathrm{m\,s^{-2}}$ during 0.44 s until it reaches a final velocity of $V_a = 0.45\,\mathrm{m\,s^{-1}}$ (blue line). The small circle indicates the end of the acceleration phase (A) of the motion; the plate motion continues at constant velocity during the relaxation phase (R). The black lines represent the work performed by the quasisteady drag force F_{QS} (— — —), the added-mass force F_{AM} (· · · · ·) and $F_{QS} + F_{AM}$ (– · –). The red dashed line (— — —) represents the work performed by $F_{QS} + F_a$, where F_a is given by (3.1). The green dashed line (— — —) shows the measured total kinetic energy of the flow from PIV velocity data.

During the relaxation phase, at $t^* \approx 2$, the work predicted by the model starts to diverge from the measured acceleration drag force. We already saw in figure 6 that the acceleration drag force $F_a(t)$ predicted by the model during the relaxation phase of the motion eventually decays slower than the measured drag force. This also explains the deviation of the work during the relaxation phase. It should be noted (as explained in § 2.1) that in the case of a circular plate, the drag force $F_D(t)$ during the relaxation phase, when the plate moves at constant velocity, would even drop below the stationary drag force given by F_{QS} (Fernando & Rival 2016). This drop in drag force is not included in the generation of the red dashed line in figure 19.

References

Al-Arabi, M. & El-Riedy, M.K. 1976 Natural convection heat transfer from isothermal horizontal plates of different shapes. *Intl J. Heat Mass Transfer* **19**, 1399–1404.

Batchelor, G.K. 1967 *An Introduction to Fluid Mechanics*. Cambridge University Press.

Biesheuvel, A. & Hagmeijer, R. 2006 On the force on a body moving in a fluid. *Fluid Dyn. Res.* **38**, 716–742.

Blevins, R.D. 2003 *Applied Fluid Dynamics Handbook*. Krieger Publishing Company.

Brennen, C.E. 1982 A review of added mass and fluid inertial forces. *Tech. Rep.* CR. 82.010. Naval Civil Engineering Laboratory, Port Hueneme, CA.

Burgers, J.M. 1921 On the resistance of fluids and vortex motion. *Proc. K. Ned. Akad. Wet.* **23**, 774–782.

Corkery, S.J., Babinsky, H. & Graham, W.R. 2019 Quantification of added-mass effects using particle image velocimetry data for a translating and rotating flat plate. *J. Fluid Mech.* **870**, 492–518.

Corkery, S.J., Stevens, P.R.R.J. & Babinsky, H. 2017 Low Reynolds numer surge response of a flat plate wing at 90 degrees incidence. In 55th AIAA Aerospace Sciences Meeting, pp. 0330.

Crank, J. 1975 *The Mathematics of Diffusion*, 2nd edn. Clarendon Press.

Crowe, C.T. 2012 *Multiphase Flows with Droplets and Particles*, 2nd edn. CRC Press.

DABIRI, J.O. 2009 Optimal vortex formation as a unifying principle in biological propulsion. *Annu. Rev. Fluid Mech.* **41**, 17–33.
DICKINSON, M.H., LEHMANN, F.-O. & SANE, S.P. 1999 Wing rotation and the aerodynamic basis of insect flight. *Science* **284**, 1954–1960.
ELDREDGE, J.D. & JONES, A.R. 2019 Leading-edge vortices: mechanics and modeling. *Annu. Rev. Fluid Mech.* **51**, 75–104.
EMANUEL, G. 2000 *Analytical Fluid Dynamics*, 2nd edn. CRC Press.
FERNANDO, J.N. & RIVAL, D.E. 2016 Reynolds-number scaling of vortex pinch-off on low-aspect-ratio propulsors. *J. Fluid Mech.* **799**, R3.
FERNANDO, J.N., WEYMOUTH, G.D. & RIVAL, D.E. 2020 On the limits of added-mass theory in separated flows and with varying initial conditions. *J. Fluids Struct.* **93**, 102835.
FREYMUTH, P., BANK, W. & PALMER, M. 1983 Visualization of accelerating flow around an airfoil at high angles of attack. *Z. Flugwiss. Weltraumforsch.* **7**, 392–400.
GALLER, J.N., WEYMOUTH, G.D. & RIVAL, D.E. 2021 On the concept of energized mass: a robust framework for low-order force modeling in flow past accelerating bodies. *Phys. Fluids* **33**, 057103.
GEHLERT, P., ANDREU-ANGELO, I. & BABINSKY, H. 2023 Vortex force decomposition—forces associated with individual elements of a vorticity field. *Exp. Fluids* **64**, 112.
GHARIB, M., RAMBOD, E. & SHARIFF, K. 1998 A universal time scale for vortex ring formation. *J. Fluid Mech.* **360**, 121–140.
GRIFT, E.J., TUMMERS, M.J. & WESTERWEEL, J. 2021 Hydrodynamics of rowing propulsion. *J. Fluid Mech.* **918**, A29.
GRIFT, E.J., VIJAYARAGAVAN, N.B., TUMMERS, M.J. & WESTERWEEL, J. 2019 Drag force on an accelerating submerged plate. *J. Fluid Mech.* **866**, 369–398.
HINTON, E.M., LEONARD, A., PULLIN, D.I. & SADER, J.E. 2024 Starting vortices generated by an arbitrary solid body with any number of edges. *J. Fluid Mech.* **987**, A11.
HOERNER, S.F. 1965 *Fluid-Dynamic Drag*. Hoerner Fluid Dynamics.
KOUMOUTSAKOS, P. & SHIELS, D. 1996 Simulations of the viscous flow normal to an impulsively started and uniformly accelerated flat plate. *J. Fluid Mech.* **328**, 177–227.
LI, Z., CHEN, L., XIANG, Y. & LIU, H. 2024 Two independent mechanisms with distinct laws for the generation of drag force on accelerating plates. *Phys. Fluids* **36**, 107163.
LI, Z., XIANG, Y., QIN, S., LIU, H. & WANG, F. 2022 Two models and the generation mechanisms of the drag on an accelerating starting disc. *Phys. Fluids* **34**, 081908.
LIGHTHILL, J. 1986 Fundamentals concerning wave loading on offshore structures. *J. Fluid Mech.* **173**, 667–681.
LIMACHER, E., MORTON, C. & WOOD, D. 2018 Generalized derivation of the added-mass and circulatory forces for viscous flows. *Phys. Rev. Fluids* **3**, 014701.
LOVALENTI, P.M. & BRADY, J.F. 1993 The hydrodynamic force on a rigid particle undergoing arbitrary time-dependent motion at small Reynolds-number. *J. Fluid Mech.* **256**, 561–605.
MANCINI, P., MANAR, F., GRANLUND, K., OL, M.V. & JONES, A.R. 2015 Unsteady aerodynamic characteristics of a translating rigid wing at low Reynolds number. *Phys. Fluids* **27**, 123102.
MCPHADEN, C.J. & RIVAL, D.E. 2018 Unsteady force estimation using a Lagrangian drift-volume approach. *Exp. Fluids* **59**, 64.
MEI, R.W. & ADRIAN, R.J. 1992 Flow past a sphere with an oscillation in the free-stream velocity and unsteady drag at finite Reynolds-number. *J. Fluid Mech.* **237**, 323–341.
MILLS, A.F. & COIMBRA, C.F.M. 2015 *Basic Heat and Mass Transfer*, 3rd edn. Temporal Publishing.
MORISON, J.R., O'BRIEN, M.P., JOHNSON, J.W. & SCHAAF, S.A. 1950 The force exerted by surface waves of piles. *J. Petrol. Technol.* **2**, 149–154.
MORTON, B.R. 1984 The generation and decay of vorticity. *Geophys. Astrophys. Fluid Dyn.* **28**, 277–308.
NOCA, F., SHIELDS, D. & JEON, D. 1997 Measuring instantaneous forces on bodies using only velocity field and their derivatives. *J. Fluids Struct.* **11**, 345–350.
ODAR, F. & HAMILTON, W.S. 1964 Forces on a sphere accelerating in a viscous fluid. *J. Fluid Mech.* **18**, 302–314.
PAYNE, P.R. 1981 The virtual mass of a rectangular flat-plate of finite aspect ratio. *Ocean Engng* **8**, 541–545.
PITT FORD, C.W. & BABINSKY, H. 2013 Lift and the leading-edge vortex. *J. Fluid Mech.* **720**, 280–313.
PRANDTL, L. 1936 Entstehung von Wirbeln bei Wasserströmungen - 1. Entstehung von Wirbeln und künstliche Beeinflussung der Wirbelbildung. Reichsanstalt für Film und Bild in Wissenschaft und Unterricht (RWU). Available at: https://doi.org/10.3203/IWF/C-1#t=05:48,08:16.
PULLIN, D.I. & SADER, J.E. 2021 On the starting vortex generated by a translating and rotating flat plate. *J. Fluid Mech.* **906**, A9.

PULLIN, D.I. & WANG, Z.J. 2004 Unsteady forces on an accelerating plate and application to hovering insect flight. *J. Fluid Mech.* **509**, 1–21.

REIJTENBAGH, J., TUMMERS, M.J. & WESTERWEEL, J. 2023 Drag force on a starting plate scales with the square root of acceleration. *Phys. Rev. Lett.* **130**, 174001.

RINGUETTE, M.J., MILANO, M. & GHARIB, M. 2007 Role of the tip vortex in the force generation of low-aspect-ratio normal flat plates. *J. Fluid Mech.* **581**, 453–468.

SADER, J.E., HOU, W., HINTON, E.M., PULLIN, D.I. & COLONIUS, T. 2024 The starting vortices generated by bodies with sharp and straight edges in a viscous fluid. *J. Fluid Mech.* **992**, A15.

SCHLICHTING, H. & GERSTEN, K. 2000 *Boundary-Layer Theory*, 8th edn. Springer.

VON KÁRMÁN, T. 1929 The impact on seaplane floats during landing. *Tech. Rep.* 321. NACA.

WANG, C.J. & ELDREDGE, J.D. 2013 Low-order phenomenological modeling of leading-edge vortex formation. *Theor. Comput. Fluid Dyn.* **27**, 577–598.

WEST, G.S. & APELT, C.J. 1982 The effects of tunnel blockage and aspect ratio on the mean flow past a circular cylinder with Reynolds numbers between 10^4 and 10^5. *J. Fluid Mech.* **114**, 361–377.

WESTERWEEL, J. & SCARANO, F. 2005 Universal outlier detection for PIV data. *Exp. Fluids* **39**, 1096–1100.

WU, J.C. 1981 Theory for aerodynamic force and moment in viscous flows. *AIAA J.* **19**, 432–441.

XU, L. & NITSCHE, M. 2014 Scaling behaviour in impulsively started viscous flow past a finite flat plate. *J. Fluid Mech.* **756**, 689–715.

XU, L. & NITSCHE, M. 2015 Start-up vortex flow past an accelerated flat plate. *Phys. Fluids* **27**, 033602.

YU, Y.T. 1945 Virtual masses of rectangular plates and parallelepipeds in water. *J. Appl. Phys.* **16**, 724–729.